行政院國家科學委員會專題研究計畫 成果報告

多重網格法與保結構二次特徵值問題計算對預測壓電材料裂縫成長的重要性
研究成果報告(精簡版)

計 畫 類 別 ：個別型
計 畫 編 號 ：NSC 97-2119-M-009-006-
執 行 期 間 ：97 年 08 月 01 日至 98 年 07 月 31 日
執 行 單 位 ：國立交通大學應用數學系（所）

計 畫 主 持 人：吳金典

計畫參與人員：碩士級-專任助理人員：黃振庭
碩士班研究生-兼任助理人員：李偉任
碩士班研究生-兼任助理人員：蔡玉麟
大專生-兼任助理人員：蔣明虔

報 告 附 件 ：國外研究心得報告

處 理 方 式 ：本計畫可公開查詢

中 華 民 國 98 年 10 月 30 日

In this report, we study the corner singularity of Laplace equation. We employee the finite element (FE) discretization on three different meshes (uniform mesh, Shishkin-type mesh and adaptively refined mesh). We also investigate the multigrid convergence of the FE solutions over these three types of mesh. We observed that the singularity is well resolved and the multigrid convergence remain robust on the Shishkin-type of meshes. In the following, we first state our problem setting and followed by the numerical results we have obtained. In the end of this report, we attach a paper that is under this NSC-grant support and has been accepted for publication in the journal, Computer Physics Communications.

I. introduction:

We consider the following problem. Let Ω be a bounded polygonal domain in $\mathbb{R}^2$ with at least one re-entrant angle. Consider the Poisson equation with homogeneous Dirichlet boundary condition:

$$\begin{aligned} -\Delta u &= f \quad \text{in } \Omega \\ u &= 0 \quad \text{in } \partial\Omega, \end{aligned}$$

where $f \in L^2(\Omega)$. Let Ω be a sector of the unit disk with angle π/β,

$$\Omega := \{(r,\theta) : 0 < r < 1, 0 < \theta < \pi/\beta\}.$$

Let $v(r,\theta) = r^\beta \sin\beta\theta$. Define $u(r,\theta) = (1-r^2)v(r,\theta)$. Note that u is zero on $\partial\Omega$. By direct computing, we find

$$\begin{aligned} \Delta u &= (1-r^2)\Delta v + 2\nabla(1-r^2)\cdot\nabla v + v\Delta(1-r^2) \\ &= -4r\frac{\partial v}{\partial r} - 4v = -(4\beta+4)v. \end{aligned}$$

To solve this problem , we use the Finite Element method with piecewise linear function on a quasi-uniform grid. It is well-known, the FE solutions convergence is of the order $O(h^2)$ in the L^2-norm and is of order $O(h)$ in H^1-norm, when $0<\theta<\pi$,where h is the mesh size of the triangulation. When the angle is over π, the convergence rates become $O(h^{1+(\pi/\theta)-\varepsilon})$ in L^2-norm and $O(h^{(\pi/\theta)-\varepsilon})$ in H^1-norm. (cf.[1] S.C. BRENNER and L.-Y.SUNG 1997)

In the following ,we introduce three different mesh discretization strategies (1)

global refinement on uniform grids , global refinement on Shishkin-type grids and adaptive local refinement on uniform grids. The uniform grid is constructed by giving uniformly distributed boundary nodes and the Shishkin type of grid is constructed by giving uniformly distributed nodes for the boundary segments on unit circle (x,y) and exponentially spacing nodes for the boundary segments that intersect with the origin, $(x, y) = (2^{-i},\ 0)$ and $(x, y) = (0\ ,\ 2^{-i}), i = 1 \cdots 10.$. The local refined grid is constructed by refining the triangles inside circular regions centered at (0,0) with radius $r = 2^{-i}$ at ith refinement step.

Four cases with different angles, $\theta = \frac{\pi}{2}, \theta = \frac{3\pi}{2}, \theta = \frac{7\pi}{4}$ and $\theta = \frac{\pi}{0.51}$, are considered in this study. The convergence rates are shown in section 3.

II. Multigrid algorithm:

It is well known that multigrid convergence rate is mesh independent for the solutions of laplace equations when the exact solution has H^2 regularity. On the non-convex domain due to the corner singularity, the order of regularity of the exact solution is decreased when the angle θ approaches to 2π. Therefore, we suspect the convergence rate of the MG algorithm will be deteriorated due to lack of regularity. On the other hand, it has been shown uniform convergence can be obtained on Shishkin meshes. We are interested in the change of the convergence rate of MG for FE solutions obtained on Shichkin type of meshes. The results shown in section 3 seem to partially support our conjectures.

$V^h \leftarrow MV^h(v^h, f^h)$

1. Relax υ_1 times on $A^h u^h = f^h$ with a given initial guess v^h.
2. If Ω^h = coarsest grid, then go to 4.

   Else $f^{2h} \leftarrow I_h^{2h}(f^h - A^h V^h)$

   $v^{2h} \leftarrow 0$
   $v^{2h} \leftarrow MV^{2h}(v^{2h}, f^{2h})$
3. Correct $v^h \leftarrow v^h + I_{2h}^h v^{2h}$.
4. Relax υ_2 times on $A^h u^h = f^h$ with initial guess v^h.

III. NUMERICAL EXPERIMENTS

Errors for each studied case over different meshes

Case1: $\theta = \frac{\pi}{2}$

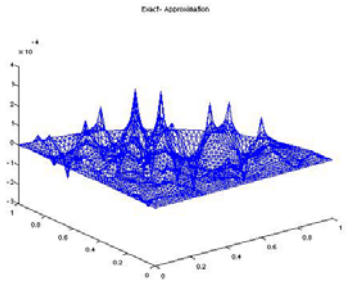

Global refinement
with Uniform Grid
# of points = 2205

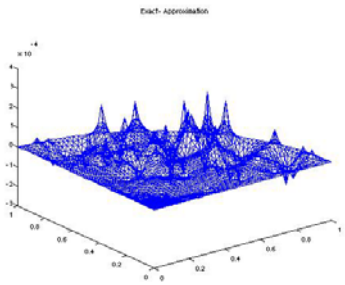

Global refinement
with Exponential Grid
# of points = 4141

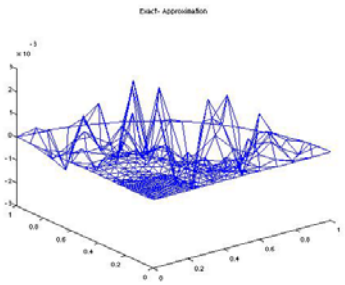

Local refinement
with Uniform Grid
# of points = 395

Mesh after two refinement steps

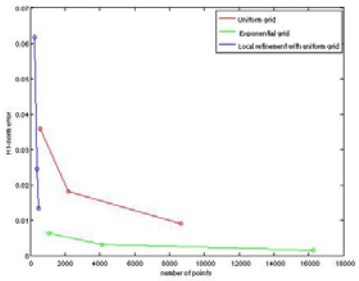

H1-norm error

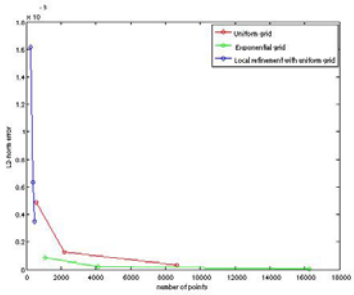

L2-norm error

	Uniform grid	Exponential grid	Local refinement
H1-norm error	8.9947e-03	1.5804e-03	1.3345e-02
L2-norm error	3.0879e-05	5.3535e-06	3.4720e-04

Comparison of the errors in L2-norm and H1-norm

Case2: $\theta = \frac{3\pi}{2}$

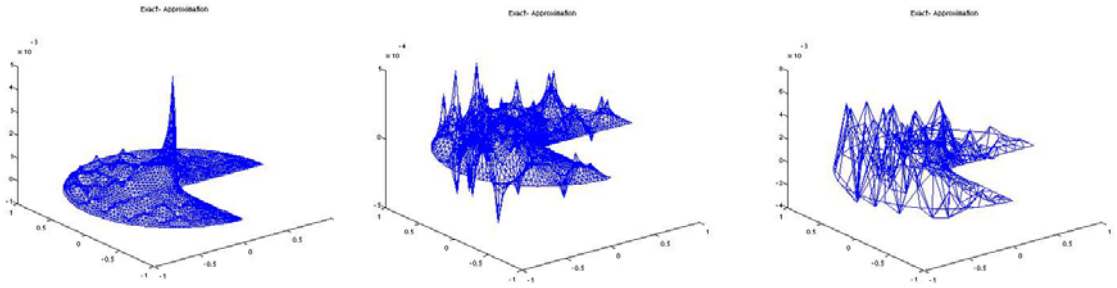

Global refinement with Uniform Grid # of points = 2331	Global refinement with Exponential Grid # of points = 8035	Local refinement with Uniform Grid # of points = 542

Mesh after two refinement steps

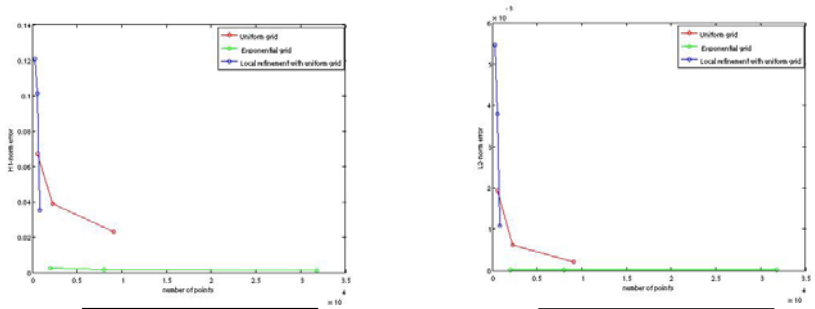

H1-norm error

L2-norm error

	Uniform grid	Exponential grid	Local refinement
H1-norm error	2.2874e-02	1.0294e-03	3.5174e-02
L2-norm error	2.0982e-04	9.0754e-07	1.08587e-03

Comparison of the errors in L2-norm and H1-norm

Case3 $\theta = \frac{7\pi}{4}$

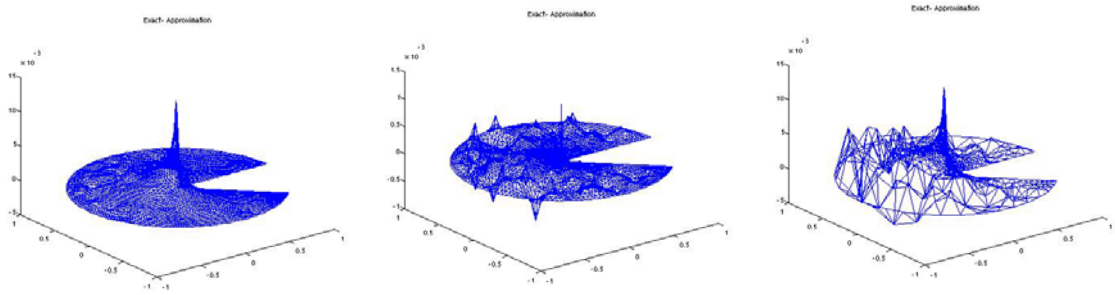

Global refinement with Uniform Grid # of points = 2733	Global refinement with Exponential Grid # of points = 9001	Local refinement with Uniform Grid # of points = 638

Mesh after two refinement steps

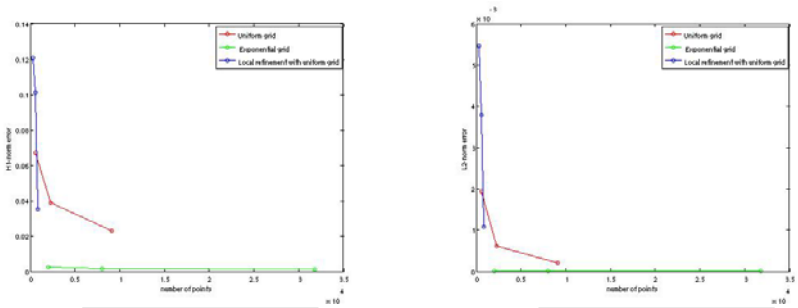

H1-norm error | L2-norm error

	Uniform grid	Exponential grid	Local refinement
H1-norm error	3.7770e-02	3.0113e-03	8.2655e-02
L2-norm error	4.8478e-04	1.2823e-06	1.8493e-03

Comparison of the errors in L2-norm and H1-norm

Case4: $\theta = \dfrac{\pi}{0.51}$

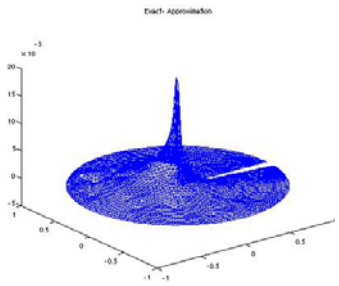

Global refinement
with Uniform Grid
# of points = 2733

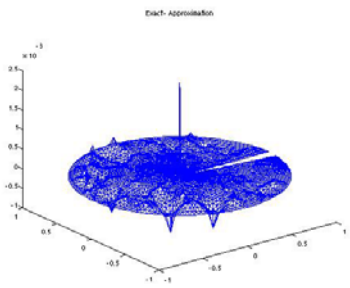

Global refinement
with Exponential Grid
# of points = 9001

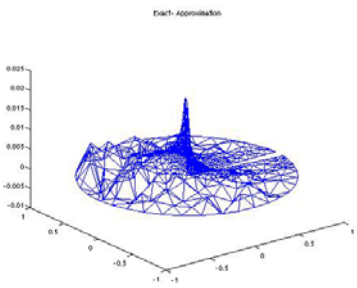

Local refinement
with Uniform Grid
# of points = 638

Mesh after two refinement steps

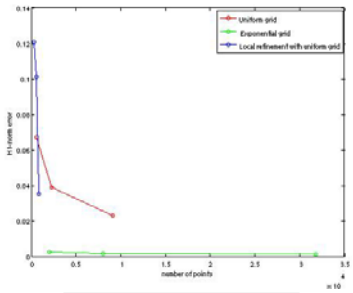

H1-norm error

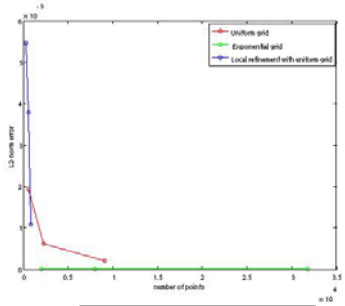

L2-norm error

	Uniform grid	Exponential grid	Local refinement
H1-norm error	5.5442e-02	1.0081e-02	1.0536e-01
L2-norm error	1.0163e-03	3.4695e-06	2.2186e-03

Comparison of the errors in L2-norm and H1-norm

The following tables show the comparisons of the theoretical convergence rate and the numerical convergence rate. Due to our limited computer facilities, only solutions on 3 levels of meshes are presented. The results in tables 1 show that the numerical convergence rate approaches to theoretical rate when the meshes are refined. However, the numerical convergence rate is away from the theoretical rate when meshes are refined for the case $\theta > \pi$. This is again due the the lack of regularity since the duality argument can only be applied when the solution has H2-regularity. On the other hand, results in table 2 show that the numerical convergence rate is very close to the theoretical rate.

Table 1.

		Theorem ratio	Numerical ratio	
			Ω^{4h}/Ω^{2h}	Ω^{2h}/Ω^{h}
$\theta=\frac{\pi}{2}$	H1	2	1.99e+000	1.99e+000
	L2	4	3.96e+000	3.98e+000
$\theta=\frac{3\pi}{2}$	H1	1.58e+000	1.73e+000	1.69e+000
	L2	3.17e+000	3.16e+000	2.92e+000
$\theta=\frac{7\pi}{4}$	H1	1.48e+000	1.56e+000	1.53e+000
	L2	2.97e+000	2.54e+000	2.36e+000
$\theta=\frac{\pi}{0.51}$	H1	1.42e+000	1.47e+000	1.44e+000
	L2	2.84e+000	2.20e+000	2.10e+000

Convergence rates on uniform grids

Table 2.

		Theorem ratio	Numerical ratio	
			Ω^{4h}/Ω^{2h}	Ω^{2h}/Ω^{h}
$\theta=\frac{\pi}{2}$	H1	2	1.9918e+000	1.9972e+000
	L2	4	3.9692e+000	3.9894e+000
$\theta=\frac{3\pi}{2}$	H1	1.5874e+000	1.5889e+000	1.5896e+000
	L2	3.1748e+000	3.9728e+000	3.9750e+000
$\theta=\frac{7\pi}{4}$	H1	1.4859e+000	1.4875e+000	1.4872e+000
	L2	2.9719e+000	3.8042e+000	3.5717e+000
$\theta=\frac{\pi}{0.51}$	H1	1.4240e+000	1.4077e+000	1.4149e+000
	L2	2.8481e+000	3.2769e+000	2.7269e+000

Convergence rates on Shishkin-type of grids

Multigrid convergence

(1) MG convergence on uniform grids

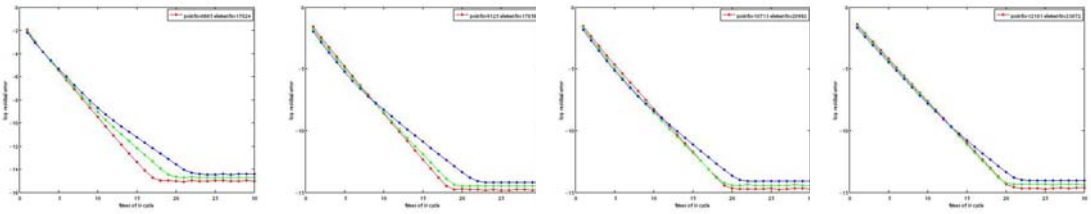

$\theta = \frac{\pi}{2}$ $\theta = \frac{3\pi}{2}$ $\theta = \frac{7\pi}{4}$ $\theta = \frac{\pi}{0.51}$

(2) MG convergence on Shishkin-type of grids

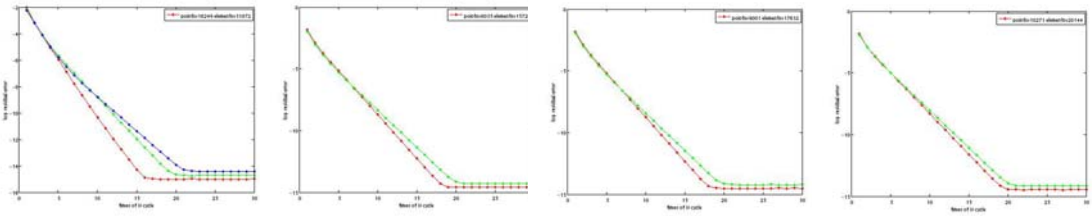

$\theta = \frac{\pi}{2}$ $\theta = \frac{3\pi}{2}$ $\theta = \frac{7\pi}{4}$ $\theta = \frac{\pi}{0.51}$

(3) MG convergence on locally refined grids

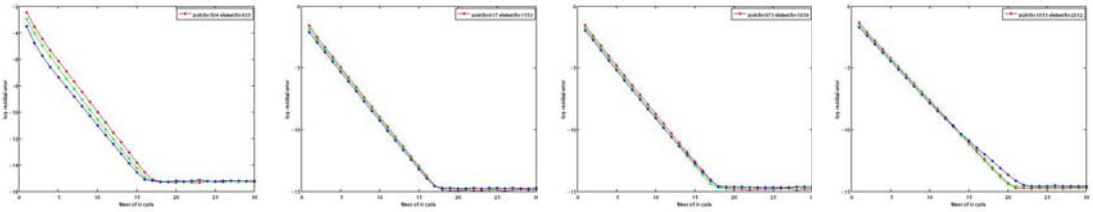

$\theta = \frac{\pi}{2}$ $\theta = \frac{3\pi}{2}$ $\theta = \frac{7\pi}{4}$ $\theta = \frac{\pi}{0.51}$

*Red line represents the convergence history on the grid Ω^{4h}.

*Green line represents the convergence history on the grid Ω^{2h}.

*Blue line represent the convergence history on the fine grid Ω^{h}.

From the above figure, one can easily see that MG convergence remains mesh independent on three types of grid.

Momentum-time flux conservation method for one-dimensional wave equations

Zhen-Ting Huang [1],Huan-Chun Hsu [2],Chau-Lyan Chang[3],Chin-Tien Wu [1], and T.F. Jiang [2,4*]

[1] *Institute of Mathematical Modeling and Scientific Computing, National Chiao-Tung University, Hsinchu 30010, Taiwan*

[2] *Institute of Physics, National Chiao-Tung University, Hsinchu 30010, Taiwan*

[3] *Computational Aerosciences Branch, NASA Langley Research Center, Hampton, VA 23681-2199, USA*

[4] *Center for Quantum Science and Engineering, National Taiwan University, Taipei 10617 , Taiwan*

(Dated: September 22, 2009)

Abstract

We present a conservation element solution element method in time and momentum space. Several paradigmatic wave problems including simple wave equation, convection-diffusion equation, driven harmonic oscillating charge and nonlinear Korteweg-de Vries (KdV) equation are solved with this method and calibrated with known solutions to demonstrate its use. With this method, time marching scheme is explicit, and the non-reflecting boundary condition is automatically fulfilled. Compared to other solution methods in coordinate space, this method preserves the complete information of the wave during time evolution which is an useful feature especially for scattering problems.

PACS numbers: 02.70.-c, 02.60.Lj

*Electronic address: tfjiang@faculty.nctu.edu.tw

I. INTRODUCTION

In the early 90's, Chang *et al.* first introduced the idea of space-time flux conservation to solving the general wave problems [1], later coined the *conservation element and solution element* (CESE) method. Since its inception, the CESE method has shown distinguished power in solving wave equations in various fields, notable examples including problems in computational fluid dynamics, aeroacoustics, electromagnetism and magnetohydrodynamics, etc. [2]. In the CESE method, the *space* degree and the *time* degree of freedom are treated in an unified way. The space-time domain is discretized into solution elements (SE), and the non-overlap space-time cells bounded by SE are called the conservation elements (CE), as depicted in Fig. 1. In each CE, the space-time flux conservation law is enforced, from which the time marching scheme is derived. The nonreflecting boundary condition (NRBC) [3] is naturally implied by applying the flux conservation idea at the boundary CE, requires no filter function, absorbing potential, etc. [4] near the boundary to keep the numerical region from being contaminated by the aliased reflection at the numerical boundary.

However, there is a general problem in coordinate space calculations : the correct information is obtained in the model numerical region, but the part of wave outside of the numerical region which are of interest in some physics problems, is lost. For example, in the problem of highly excited states or the photoionized electron spectrum, the wave function extends to a very large spatial range, making calculations in coordinate space intractable. Theoretically, the coordinate space and the momentum space representations are equivalent and complementary to each other in case the solution is complete. This complementarity implies that a widely diffusive wave in coordinate space will correspond to a narrowly localized one in momentum space, and because momentum is directly related to kinetic energy, extremely large momentum for a system would usually be unphysical. Thus a moderate momentum region will be sufficient for a numerical modeling of complete information. Also, the wave will simply vanish at the numerical boundary and cause no trouble like methods in coordinate space. Naturally, solving problems in momentum space was attempted, yet difficulties such as singularity in Coulombic system are usually encountered [5]. Some method such as Lande regularization was proposed to resolve that singularity, but the range of momentum space must be unreasonably large to produce correct eigenstates, causing a disadvantage in practice. Recently we found that the controversy can easily be resolved by

taking the numerical finite coordinate range into consideration in constructing the momentum space representation. With this recipe, we have efficiently calculated the photoelectron spectra of hydrogen atom under intense laser pulses [6].

In this paper, we aim to develop a new momentum space CESE (p-CESE) method that preserves the power of CESE and keeps the complete information of the solution simultaneously during time evolution. A Fourier transformation can convert the momentum space solution into coordinate space representation at any time if information in the latter is requested, making the momentum space approach useful for time-dependent systems and scattering problems. This paper contains the layout of the fundamental ideas of the p-CESE method and justification of this new method by calculating the analytic solutions of some paradigmatic wave equations. The development covered classical, quantum mechanical and nonlinear wave problems. The extension to higher dimensional systems will be reported in future work. The rest of the paper is organized as follows : In Sec. II, we present the formulation of the p-CESE method for the simple wave equation. In Sec. III, we treat the convection-diffusion equation. In Sec. IV, we calculate the time-dependent Schrödinger equation of a driven harmonically oscillating charge. And in Sec. V, the nonlinear Korteweg-de Vries (KdV) equation was solved by p-CESE method. Discussion and conclusions are given in Sec. VI.

II. SIMPLE WAVE EQUATIONS AND THE FORMULATION OF MOMENTUM SPACE CESE METHOD

Consider first the simple wave equation

$$\frac{\partial u}{\partial t} + a\frac{\partial u}{\partial x} = 0, \tag{1}$$

where the wave speed a is a constant. The solution of $u(x,t)$ is in the form of $f(x-at)$ with a shape function f. For positive a, the wave will move toward the positive x direction. Because the numerical range of x is finite, eventually the wave front will reach the numerical boundary in sufficiently long time. The treatment in coordinate space will encounter difficulties if the wave at large distance is important, such as in the scattering state problem. This simple system was employed in Ref. [1] to develop the basic CESE method and was named the a-scheme. Making the following Fourier transformations, the system has the coordinate and

the momentum representation alternatively :

$$\begin{aligned} u(x,t) &= \int \tilde{u}(p,t)\, e^{ipx} dp, \\ \tilde{u}(p,t) &= \frac{1}{2\pi} \int u(x,t)\, e^{-ipx} dx, \end{aligned} \tag{2}$$

the wave equation in momentum representation becomes

$$\frac{\partial \tilde{u}(p,t)}{\partial t} = -iap\, \tilde{u}(p,t). \tag{3}$$

This is simply an ordinary differential equation. With initial condition $\tilde{u}(p, t = 0)$, the solution at any time is

$$\tilde{u}(p,t) = \tilde{u}(p,t=0)\, e^{-ipat}. \tag{4}$$

Obviously, the amplitude of the solution $\tilde{u}(p,t)$ is stationary at any time in the momentum space. Though the equation and its solution in momentum space are rather simple, they serve the development as a calibration example for the p-CESE method. Following the formalism of the a-scheme in coordinate space CESE [1], we derive the a-scheme of p-CESE method below. We define the two-dimensional Euclidean space $(x_1, x_2) \equiv (p, t)$, $\nabla \equiv (\partial/\partial p, \partial/\partial t)$ and the two-dimensional vector $\mathbf{h} \equiv (h_1, h_2) = (0, \tilde{u})$. Then, Eq.(3) becomes

$$\nabla \cdot \mathbf{h} = -ipa\, \tilde{u}(p,t). \tag{5}$$

The momentum-time $(p-t)$ space is discretized with the staggered SEs and nonoverlapping CEs similarly as described in Ref. [1] except the coordinate x is now the momentum p. For completeness, the $p-t$ space is drawn in Fig. 1. Associated with each $p-t$ mesh point (p_j, t^n), designated as (j,n), is the SE(j,n) shown as the cross line segments passing the mesh point (j,n). Conservation elements CE$_-(j,n)$ and CE$_+(j,n)$ are associated with SE(j,n). Integrating Eq.(5) over the CE$_\pm(j,n)$ and applying the divergence theorem, we have

$$\begin{aligned} \int_{CE_+} \mathbf{h} \cdot d\mathbf{s} &= \int_{CE_+} [-ipa\, \tilde{u}(p,t)] dp dt, \\ \int_{CE_-} \mathbf{h} \cdot d\mathbf{s} &= \int_{CE_-} [-ipa\, \tilde{u}(p,t)] dp dt, \end{aligned} \tag{6}$$

where $d\mathbf{s}$ is the generalized line element associated with the generalized area element $dp\, dt$, with fixed convention in the normal direction. We take $d\mathbf{s} = (dt, -dp)$, that is, the line

integral in each CE is calculated counterclockwise. For the left-hand side of Eqs.(6), the line integrals along t segments are null because $\mathbf{h} \cdot d\mathbf{s} = -\tilde{u}\, dp$, which has no component in the t-direction. For any (p,t) lying on SE(j,n), $\tilde{u}(p,t)$ and $\mathbf{h}(p,t)$ are expanded at $\tilde{u}(p,t;j,n)$ and $\mathbf{h}(p,t;j,n)$ up to the first order, respectively

$$\begin{aligned} \tilde{u}(p,t;j,n) &\simeq \tilde{u}_j^n + (\tilde{u}_p)_j^n (p-p_j) + (\tilde{u}_t)_j^n (t-t^n), \\ \mathbf{h}(p,t;j,n) &\simeq (0, \tilde{u}(p,t;j,n)), \end{aligned} \tag{7}$$

where (j,n) denotes the mesh point (p_j, t^n) . With the expansion, it is seen that on the space-time mesh grids,

$$(\tilde{u}_t)_j^n = -i\, a\, p_j\, \tilde{u}_j^n. \tag{8}$$

By Eqs. (7), the flux conservation Eqs. (6) become

$$\tilde{u}_j^n \pm (\tilde{u}_{\bar{p}})_j^n - \left[\tilde{u}_{j\pm\frac{1}{2}}^{n-\frac{1}{2}} \mp (\tilde{u}_{\bar{p}})_{j\pm\frac{1}{2}}^{n-\frac{1}{2}}\right] = -i\, a\, p_{j\pm\frac{1}{4}} \frac{\Delta t}{2}\, \tilde{u}_{\pm}^*, \tag{9}$$

where we designate $\tilde{u}_{\bar{p}} = \frac{\Delta p}{4} \cdot \tilde{u}_p$. $\tilde{u}_{\pm}^*$ denotes the mean value of $\tilde{u}$ in the integrand of the area integrals of Eqs. (6) such that

$$\int_{CE_{\pm}} [-ipa\, \tilde{u}(p,t)] dp dt = -i\, a\, p_{j\pm\frac{1}{4}} \frac{\Delta t \cdot \Delta p}{4}\, \tilde{u}_{\pm}^*, \tag{10}$$

for CE$(j,n)_{\pm}$, respectively. Since $\tilde{u}_{\pm}^*$ are not located on our mesh grids, we develop a convenient numerical iteration scheme for time marching. Let the index ℓ indicate the iteration level of convergence. In the first step, $\tilde{u}_{\pm}^*$ is approximated by $\tilde{u}_{j\pm\frac{1}{4}}^{n-\frac{1}{2}}$; after the initial step, $\tilde{u}_{j\pm\frac{1}{4}}^{n}$ is employed as the new input $\tilde{u}_{\pm}^*$. Although these $\tilde{u}_{\pm}^*$ are not on the mesh grids, they are in the solution elements and Eq. (7) can be used. The iteration scheme goes as follows :

$$\tilde{u}_{j,\ell}^n \pm (\tilde{u}_{\bar{p}})_{j,\ell}^n - \left[\tilde{u}_{j\pm\frac{1}{2}}^{n-\frac{1}{2}} \mp (\tilde{u}_{\bar{p}})_{j\pm\frac{1}{2}}^{n-\frac{1}{2}}\right] = -i\, a\, p_{j\pm\frac{1}{4}} \frac{\Delta t}{2}\, \tilde{u}_{\pm,\ell-1}^*. \tag{11}$$

The iteration is stopped if the convergence criterion

$$\left|\tilde{u}_{j,\ell+1}^n - \tilde{u}_{j,\ell}^n\right| < \varepsilon \tag{12}$$

is satisfied for a plausibly small ϵ, which is usually matched within ten iterations. The time-marching scheme developed above is explicit. From the known $\tilde{u}_{j\pm1/2}^{n-1/2}$ and $(\tilde{u}_{\bar{p}})_{j\pm1/2}^{n-1/2}$ at time level $n-1/2$, we can solve for unknowns $\tilde{u}_j^n$ and $(\tilde{u}_{\bar{p}})_j^n$ at subsequent time level n. A time step Δt consists of two half-time steps $\frac{1}{2}\Delta t$ as in the original CESE method [1].

For testing, we set $a = 1$ and study the following traveling Gaussian wave packet and its Fourier transform :

$$\begin{aligned} u(x,t) &= e^{-\frac{1}{2}(x-t)^2}, \\ \tilde{u}(p,t) &= \frac{1}{\sqrt{2\pi}} e^{-ipt-\frac{p^2}{2}}. \end{aligned} \tag{13}$$

As a comparison, we perform the coordinate space CESE a-scheme with the range $-5 \leq x \leq 5$. In Fig. 2 we show the calculated and analytic solutions at $t = 1$ and at $t = 5$. For the case of $t = 1$, the wave is still wholly inside the numerical region; for the case of $t = 5$, part of the wave has already flowed out of the coordinate space. The NRBC derived from flux conservation automatically gives a smooth leakage of wave through the numerical boundary without causing aliased reflection error.

Next we calculate the same wave equation through the developed a-scheme of the p-CESE method using $\Delta p = 0.16, \Delta t = 0.08$ and the Courant number 0.5. Fig. 3 shows the real part and the imaginary part of the analytic and computed waves at $t = 5$. Note that $|\tilde{u}(p,t)| = e^{-\frac{p^2}{2}}$, thus the momentum space solution at the boundary is equal to $e^{-12.5} = 3.7 \times 10^{-6}$ times of its peak value at $p = 0$, appropriate to be considered as vanishing. Therefore we can take the momentum space wave as stationary with no flow out of the numerical region. The behavior of computational errors will be discussed in the section of KdV equation later, but basically the error is visually invisible. The results of this section imply that for a traveling wave, the momentum space method contains more complete information than the coordinate space method, and the formulation of the new p-CESE method is justified.

III. CONVECTION-DIFFUSION EQUATIONS

Next, we consider the convection-diffusion equation :

$$\frac{\partial u}{\partial t} + a\frac{\partial u}{\partial x} - \mu\frac{\partial^2 u}{\partial x^2} = 0, \tag{14}$$

where the wave velocity a, and the viscosity coefficient μ are constants, called the μ-scheme in the CESE framework [1]. By Fourier transformation, Eq. (14) can be transformed into the momentum space form,

$$\frac{\partial \tilde{u}}{\partial t} + \left(i\,a\,p + \mu\,p^2\right)\,\tilde{u} = 0. \tag{15}$$

Applying the Gauss divergence theorem to the two-dimensional $p-t$ space,

$$\oint_{S(\mathrm{CE}_{\pm}(j,n))} \mathbf{h}\cdot d\mathbf{s} = -\int_{\mathrm{CE}_{\pm}(j,n)} \left(i\,a\,p+\mu\,p^2\right)\,\tilde{u}\,dpdt. \tag{16}$$

where $\mathbf{h}\equiv(h_1,h_2)=(0,\tilde{u})$, we can see that with $\tilde{u}=\tilde{u}(p,t;j,n)$ defined by Eq. (7), at the mesh points (j,n),

$$(\tilde{u}_t)_j^n = -\left(i\,a\,p_j+\mu\,p_j^2\right)\,\tilde{u}_j^n. \tag{17}$$

The explicit time-marching scheme is derived similarly to the previous simple wave case, that is,

$$\tilde{u}_{j,\ell}^n \pm (\tilde{u}_{\bar{p}})_{j,\ell}^n - \left[\tilde{u}_{j\pm\frac{1}{2}}^{n-\frac{1}{2}} \mp (\tilde{u}_{\bar{p}})_{j\pm\frac{1}{2}}^{n-\frac{1}{2}}\right] = -\frac{\Delta t}{2}\left(i\,a\,p_{j\pm\frac{1}{4}}+\mu\,p_{j\pm\frac{1}{4}}^2\right)\,\tilde{u}_{\pm,\ell-1}^*, \tag{18}$$

where ℓ is the iteration index and the iterative scheme is the same as described in the previous section. With the aid of Eqs. (17) and (18), the unknowns $\tilde{u}_j^n$ and $(\tilde{u}_{\bar{p}})_j^n$ can be solved iteratively in terms of known $\tilde{u}_{j\pm1/2}^{n-1/2}$ and $(\tilde{u}_{\bar{p}})_{j\pm1/2}^{n-1/2}$ in the preceding time level.

The momentum space convection-diffusion equation is also an ordinary differential equation with the general solution

$$\tilde{u}_e(p,t) = f(p)\times\exp\left[-\left(i\,a\,p+\mu\,p^2\right)t\right], \tag{19}$$

with an arbitrary shape function $f(p)$. As a calibration of the p-CESE method, we use a Gaussian shape $f(p)=\exp(-p^2)$ below. The numerical results for $a=1$ and $\mu=1$ at $t=5$ are depicted in Fig. 4, showing excellent agreements between calculated and exact solutions. As we know, solving Eq. (14) in coordinate space is not as straightforward as this momentum space approach. A $c-$scheme with numerical dissipation was implemented for the treatment in the coordinate space approach [2], while the simplest $a-$scheme in p-CESE method already gives accurate results. For a reference, the exact solution in coordinate space corresponds to Eq. (19) is

$$u(x,t) = \sqrt{\frac{\pi}{1+\mu t}}\times\exp\left[\frac{-(x-at)}{4(1+\mu t)}\right]. \tag{20}$$

IV. DRIVEN SIMPLE HARMONIC OSCILLATOR

Next we solve a quantum mechanical problem by the p-CESE method. Under the velocity gauge and the dipole approximation, a charge q oscillating in the simple harmonic potential

with applied electromagnetic pulse is described by the time-dependent Schrödinger equation

$$i\frac{\partial u}{\partial t} = \left[\frac{p^2}{2} + \frac{1}{2}\,\Omega^2\,x^2 - A(t)\cdot p\right] u. \tag{21}$$

Throughout this section, we use atomic units $\hbar = 1$, $m = 1$ and $e = 1$, thus 1 a.u. laser peak intensity equals to $7.02 \times 10^{16} watt/cm^2$. The relationship between electric field and vector potential is given by

$$E(t) = -\partial A(t)/\partial t.$$

The transition probability from the ground state $|0>$ to an excited state $|N>$ is given by Poisson's distribution [7]

$$P_{0\to N} = e^{-\sigma}\frac{\sigma^N}{N!}, \tag{22}$$

where σ is a pulse parameter

$$\sigma = \frac{1}{2\Omega}\left|\int_{\infty}^{\infty} E(t)e^{i\Omega t}dt\right|^2. \tag{23}$$

Recast Eq. (21) into p-space, we obtain

$$i\,\tilde{u}_t + \frac{1}{2}\,\Omega^2\,\tilde{u}_{pp} = \left[\frac{p^2}{2} - A(t)\cdot p\right]\tilde{u}. \tag{24}$$

With $\tilde{u} = \tilde{u}(p,t;j,n)$ and expansion of Eq. (7) at mesh point (j,n), Eq. (24) becomes

$$(\tilde{u}_t)_j^n = -i\left[\frac{p_j^2}{2} - A(t^n)\cdot p_j\right]\tilde{u}_j^n. \tag{25}$$

Furthermore, for $(p,t) \in \mathrm{SE}(j,n)$, we define

$$\mathbf{h}(p,t;j,n) = \left(\frac{1}{2}\,\Omega^2\,\tilde{u}_p(p,t;j,n), i\,\tilde{u}(p,t;j,n)\right), \tag{26}$$

and the flux theorem for $\mathrm{CE}_{\pm}(j,n)$ becomes

$$\oint_{S(\mathrm{CE}_{\pm}(j,n))} \mathbf{h}\cdot d\mathbf{s} = \int_{\mathrm{CE}_{\pm}(j,n)}\left[\frac{p^2}{2} - A(t)\cdot p\right]\tilde{u}\,dpdt. \tag{27}$$

Evaluating the area integral over $\mathrm{CE}_{\pm}(j,n)$ by the mean value method of $\tilde{u}_{\pm}^*$ as described in former sections, we obtain

$$\begin{aligned} i\left\{\tilde{u}_{j,\ell}^n \pm (\tilde{u}_{\bar{p}})_{j,\ell}^n - \left[\tilde{u}_{j\pm\frac{1}{2}}^{n-\frac{1}{2}} \mp (\tilde{u}_{\bar{p}})_{j\pm\frac{1}{2}}^{n-\frac{1}{2}}\right]\right\} \mp \frac{1}{2}\Omega^2\frac{\Delta t}{\Delta p}\left[(\tilde{u}_p)_{j,\ell}^n - (\tilde{u}_p)_{j+\frac{1}{2}}^{n-\frac{1}{2}}\right] \\ = \frac{\Delta t}{2}\left[\frac{p_{j\pm\frac{1}{4}}^2}{2} - A(t^{n-\frac{1}{4}})\cdot p_{j\pm\frac{1}{4}}\right]\times\tilde{u}_{\pm}^*. \end{aligned} \tag{28}$$

where ℓ is the iteration index, and the iteration scheme as in previous sections is applied for time marching. With the aid of Eqs. (25) and (28), the unknowns $\tilde{u}_j^n$ and $(\tilde{u}_{\bar{p}})_j^n$ can be solved iteratively in terms of the known $\tilde{u}_{j\pm1/2}^{n-1/2}$ and $(\tilde{u}_{\bar{p}})_{j\pm1/2}^{n-1/2}$ of the previous time level. As an illustration of the method, we choose a light pulse with a Sin^2 envelop,

$$E(t) = E_m \sin^2 \frac{\pi t}{T} \cos \omega t, \tag{29}$$

$$0 < t < T.$$

We assume the carrier frequency of the electric field is $\omega = 0.057$ a.u. (800 nm in wavelength), $E_m = 0.002$ a.u., and the total time duration T is 8 optical cycles. Furthermore, we assume the near resonant case, $\Omega = 0.058$ so that excitations are significant. The system is initially prepared in the ground state

$$\tilde{u}(p, t = 0) = \frac{1}{(\Omega\,\pi)^{\frac{1}{4}}} \exp\left(-\frac{p^2}{2\,\Omega}\right). \tag{30}$$

The transition probabilities $P_{0\to N}$ from the ground state to other excited state N are listed in Table I, calculated from the overlap of the final wave function $\tilde{u}(p, t = T)$ with the eigenstate $\tilde{u}_N$:

$$P_{0\to N} = \left| \int_{-\infty}^{\infty} \tilde{u}\, \tilde{u}_N^*\, dp \right|^2. \tag{31}$$

We can see that reasonably good results are obtained through the p-CESE method, and the error in each transition probability is scaled nearly to $(\Delta p)^2$ with different grids. This error behavior will be discussed in KdV system.

V. THE KORTEWEG-DE VRIES EQUATION

The *Korteweg-de Vries* (KdV) equation is a classic example of the nonlinear wave equations [8, 9]. The general form is

$$\frac{1}{\beta}\frac{\partial u}{\partial t} + \frac{\alpha}{\gamma} u \frac{\partial u}{\partial x} + \frac{1}{\gamma^3}\frac{\partial^3 u}{\partial x^3} = 0, \tag{32}$$

where α, β and γ are non-zero constants. The system contains both nonlinearity and dispersion. For convenience, we study in this section the scaled equation

$$u_t - 6u\, u_x + u_{xxx} = 0. \tag{33}$$

By Fourier transformation and some manipulations, the momentum space equation is

$$\tilde{u}(p,t)_t = 3\,i\,p\int_{-\infty}^{\infty}\tilde{u}(q,t)\,\tilde{u}(p-q,t)dq + i\,p^3\,\tilde{u}. \tag{34}$$

Let $\mathbf{h}=(0,\tilde{u})$ and applying the Gauss divergence theorem in E_2, Eq. (34) becomes

$$\oint_{S(V)}\mathbf{h}\cdot d\mathbf{s} = \int_V\left[3\,i\,p\int_{-\infty}^{\infty}\tilde{u}(q,t)\,\tilde{u}(p-q,t)\,dq + i\,p^3\,\tilde{u}\right]dpdt. \tag{35}$$

We can see that for a nonlinear system, the source terms on the right-hand side of Eq. (34) contain the convolutional integral of unknown functions, hence the straightforward explicit iteration scheme described in previous sections does not work. We implement two new ideas for the treatment of nonlinear problems in the p-CESE method. First, at each time level, we calculate $\tilde{u}(p,t)$ and $\tilde{u}_p(p,t)$ at grids of half spacings, instead of spacings at staggered Δp in linear examples. The convolutional integral can then be calculated by Simpson's rule [10]. Second, for every half-marching time step, say from $t^{n-\frac{1}{2}}$ to t^n, we begin by using $\tilde{u}$ and $\tilde{u}_p$ at $t^{n-\frac{1}{2}}$ for the source terms and find the solution at t^n, then with the obtained, we can find $\tilde{u}$ and $\tilde{u}_p$ at grids $(j\pm\frac{1}{4},n)$ through the expansion with respect to $\mathrm{SE}(j,n)$ as in Eqs. (7). These are used in the source terms to generate new solutions iteratively until the convergent criterion is satisfied. Usually the results converge within a few iterations.

In mathematical forms, from the conservation laws for $\mathrm{CE}_{\pm}(j,n)$,

$$\oint_{S(\mathrm{CE}_{\pm}(j,n))}\mathbf{h}(x,t;j,n)\cdot d\mathbf{s} = 3\,ip\int_{\mathrm{CE}_{\pm}(j,n)}\left(\int_{-\infty}^{\infty}\tilde{u}(q,t)\,\tilde{u}(p-q,t)\,dq\right)dpdt + \int_{\mathrm{CE}_{\pm}(j,n)} i\,p^3\,\tilde{u}\,dpdt, \tag{36}$$

where $\mathbf{h}(p,t;j,n)=(0,\tilde{u}(p,t;j,n))$. We can derive the following a-scheme iterations

$$\begin{aligned} u_j^n &= \frac{1}{2}\left\{[u-u_{\bar{p}}]_{j+\frac{1}{2}}^{n-\frac{1}{2}} + [u+u_{\bar{p}}]_{j-\frac{1}{2}}^{n-\frac{1}{2}}\right\} + \frac{F}{\Delta p} + \frac{G}{\Delta p},\\ u_{\bar{p}},_j^n &= \frac{1}{2}\left\{[u-u_{\bar{p}}]_{j+\frac{1}{2}}^{n-\frac{1}{2}} - [u+u_{\bar{p}}]_{j-\frac{1}{2}}^{n-\frac{1}{2}}\right\} + \frac{F}{\Delta p} - \frac{G}{\Delta p}, \end{aligned} \tag{37}$$

where we designate $u_j^n=\tilde{u}(p_j,t^n)$, $u_{\bar{p}},_j^n \equiv \frac{\Delta p}{4}(\tilde{u}_p)_j^n$, and $\Delta\tau=\frac{\Delta p}{2}\frac{\Delta t}{2}$ for shorthand. And

$$\begin{aligned} F &= \left\{3ip_{i+1/2}\sum_j u(p_{i+1/2}-q_j,t^{n-1/2})u(q_j,t^{n-1/2})\frac{\Delta p}{2} + ip_{i+1/2}^3 u(p_{i+1/2},t^{n-1/2})\right\}\Delta\tau,\\ G &= \left\{3ip_{i-1/2}\sum_j u(p_{i-1/2}-q_j,t^{n-1/2})u(q_j,t^{n-1/2})\frac{\Delta p}{2} + ip_{i-1/2}^3 u(p_{i-1/2},t^{n-1/2})\right\}\Delta\tau. \end{aligned}$$

The KdV Eq. (33) has a solitonic solution

$$u(x,t) = -\frac{c}{2}\,\mathrm{sech}^2(\frac{\sqrt{c}}{2}(x - ct + x_0)). \tag{38}$$

Note that the solution depends on the speed c of soliton and therefore multiplying the solution by an arbitrary constant is no longer a solution. Without loss of generality, we set the initial peak position at $x_0 = 0$ with the wave propagating at speed c to the right of the x-axis without shape change. The exact solution in momentum space is

$$\tilde{u}_e(p,t) = -p\,\mathrm{csch}(\frac{\pi p}{\sqrt{c}})\,\exp(-i\,pct). \tag{39}$$

Fig. 5a and 5b depict the real and the imaginary part of the numerical results together with the analytic results at time $t = 5$ and show excellent agreements between the p-CESE calculation and the analytic results.

in Fig. 6a, comparison of the magnitudes of the calculated and the exact solutions at $t = 5$ with $c = 1$ is shown. For the soliton solution, although the real part and the imaginary part oscillate with time, the magnitude is stationary as seen from Eq. (39).

The previous section has shown that our developed p-CESE method works well for various kinds of wave problems. Here we present the error analysis for this method. We define the root-mean-square error at the final moment of time as follows :

$$E(N) = \sqrt{\frac{1}{N}\sum_{j=0}^{j=N}\left[u(p_j, t^{final}) - u_{exact}\right]^2}\,. \tag{40}$$

In Table II, we listed the errors with respect to the grid size Δp and in Fig. 6b the error versus $(\Delta p)^2$ are plotted. The straight line shows that the error behaves as $\sim O(\Delta p)^2$, a general scaling behavior of our developed p-CESE a-scheme method.

VI. DISCUSSION AND CONCLUSIONS

In this paper, we developed the CESE method in momentum space on a fundamental scope and explored the solutions of several paradigmatic wave equations, namely the basic one-dimensional wave equation, the convection-diffusion equation, the driven quantum mechanical problem and the nonlinear KdV equation. In each problem, we developed an explicit time-marching scheme in the p-CESE method. While it is straightforward for linear

problems, for nonlinear problems such as the KdV equation, convolution integral of unknown functions in the source term is involved. This difficulty is resolved by employing the half-step grid size for the convolutions and the iterations during time marching. Each system was calibrated with a known exact solution, and we showed that the p-space CESE method works well for systems from classical wave equations, quantum mechanical problems to nonlinear equations, and the error behavior of the developed scheme is $\sim O(\Delta p)^2$. The main advantages of the p-CESE method, in cooperation with the superior CESE method in coordinate space, are threefold. *First,* like the original CESE method, applying the momentum-time flux conservation concept in staggered mesh, the explicit time marching scheme for every wave equation can be derived. *Second,* the boundary conditions are fulfilled automatically. That is, for a sufficient large momentum value, the wave and its derivatives are simply vanishing small at the numerical boundary, because the kinetic energy of a system is physically finite. *Third,* the information of the wave is completely preserved within the numerical momentum region, without loss at the boundary as in the coordinate space method. This will be especially useful in treating scattering problems. In this paper, we aim to develop a method for waves that extend to far distance as time goes on. This category of problems is closely related to the experimental problems such as photoelectron spectra etc.. The problem with waves extending to far distances is not easy to treat by coordinate space methods, as demonstrated in Fig. 2. We show that the p-CESE is capable for this kind of problem. On the other hand, the boundary value problems in finite domain were solved neatly by coordinate space CESE method [1], and is not our goal here. Our algorithm follows the core scheme of CESE method, and the stability criterion has been rigorously discussed [1, 11]. The criterion in our scheme is $a\,dt/dp \leq 1$. Also, in each time step, we calculate the correlation integral and the cost is $\sim O(N^2)$ for N grid points. During each time step, there is an iteration scheme for accurate computation of the correlation integral. However, the integral converges within ten iterations, so the cost is $\sim c \cdot O(N^2)$ where c is a constant of order 1. The computational cost can be compared with other conventional finite-difference schemes. Finally, for realistic problems, higher dimensional method is necessary. This problem, together with higher order of accuracy p-CESE method, is currently under development.

Acknowledgments

TFJ thanks the support of NSC, Taiwan under the contract of number NSC97-2112-M-009-002-MY3. He also acknowledges the hospitality of NASA/NIA through the MoE between NASA and NARL, Taiwan.

[1] S.C. Chang and W.M. To, *"A New Numerical Framework for Solving Conservation Laws – The Method of Space-Time Conservation Element and Solution Element,"* NASA/TM 104495 (1991); Chang, S.C. Chang, J. Comput. Phys., 119, 295 (1995).

[2] More details and references can be found in http://www.grc.nasa.gov/WWW/microbus/

[3] S.-C. Chang, A. Himansu, C.-Y. Loh, X.-Y. Wang and S.-T.J. Yu, *"Robust and Simple Non-Reflecting Boundary Conditions for the Euler Equations, A New Approach Based on the Space-Time CE/SE Method,* NASA/TMX2003-212495/REV1 (2003).

[4] See for example, Tsin-Fu Jiang and Shih-I Chu, Phys. Rev. **A**46, 7322 (1992).

[5] U.L. Pen and T.F. Jiang, Phys. Rev. A 46, 4297 (1992); and Phys. Rev. A 53, 623 (1996).

[6] See T.F. Jiang, Comp. Phys. Commun. 178, 571 (2008) and references therein.

[7] C. Cohen-Tannoudji, J. Dupont-Roc, C. Fabre, and G. Grynberg, Phys. Rev. A**8**, 2747 (1973).

[8] P.G. Drazin and R.S. Johnson, *"Solitons : an Introduction,"* (Cambridge Univ. Press, Cambridge, 1989).

[9] G.B. Arfken and H.J. Weber, *"Mathematical Methods for Physicists",* 4th Ed. Sec. 8.1 (Academic Press, San Diego, 1995).

[10] J.H. Mathews and K.D. Fink, *"Numerical Methods Using Matlab,"* 4th. Ed. Sec. 7.2 (Pearson Prentice Hall, London, 2004).

[11] Sin-Chung Chang, *On Space-Time Inversion Invariance and Its Relation to Non-dissipatedness of a CESE Core Scheme,"* AIAA paper 2006-4779 (2006).

TABLE I: Numerical results of transition probability from the ground state to state $|N>$. Also listed are the exact values and the errors. Three grid spacings $\Delta p = 0.08, 0.04$ and 0.02 were used in calculations. The time step $\Delta t = 8 \times 10^{-4}$ is used throughout.

	$P_{0\to N}$						
N	exact	$[\Delta p = 0.02$	Error]	$[\Delta p = 0.04$	Error]	$[\Delta p = 0.08$	Error]
0	0.1951894	0.1948923	-2.97(-4)	0.1940719	-1.12(-3)	0.1916537	-3.54(-3)
1	0.3188975	0.3183566	-5.41(-4)	0.3168929	-2.00(-3)	0.3130507	-5.85(-3)
2	0.2605050	0.2603970	-1.08(-4)	0.2602243	-2.81(-4)	0.2612223	7.17(-4)
3	0.1418697	0.1421716	3.02(-4)	0.1430856	1.21(-3)	0.1462422	4.37(-3)
4	0.0579461	0.0582811	3.35(-4)	0.0591675	1.22(-3)	0.0609044	2.96(-3)
5	0.0189343	0.0191296	1.95(-4)	0.0195836	6.49(-4)	0.0198997	9.65(-4)
6	0.0051558	0.0052353	7.95(-5)	0.0053896	2.34(-4)	0.0053358	1.80(-4)
7	0.0012033	0.0012287	2.54(-5)	0.0012640	6.07(-5)	0.0012595	5.62(-5)
$\sum P_{0\to N} =$	0.9997011	0.9996922		0.9996794		0.9995683	

noted : $-2.97(-4)$ denotes -2.97×10^{-4} .

TABLE II: The root-mean-square error $E[N]$ versus mesh size Δp shows $O(\Delta p^2)$ behavior for KdV equation in our p-CESE method under the a-scheme.

N	Δp	E[N]
26	0.4	5.57×10^{-2}
51	0.2	1.23×10^{-2}
101	0.1	2.94×10^{-3}
201	0.05	7.18×10^{-4}
401	0.025	1.72×10^{-4}
801	0.0125	3.57×10^{-5}

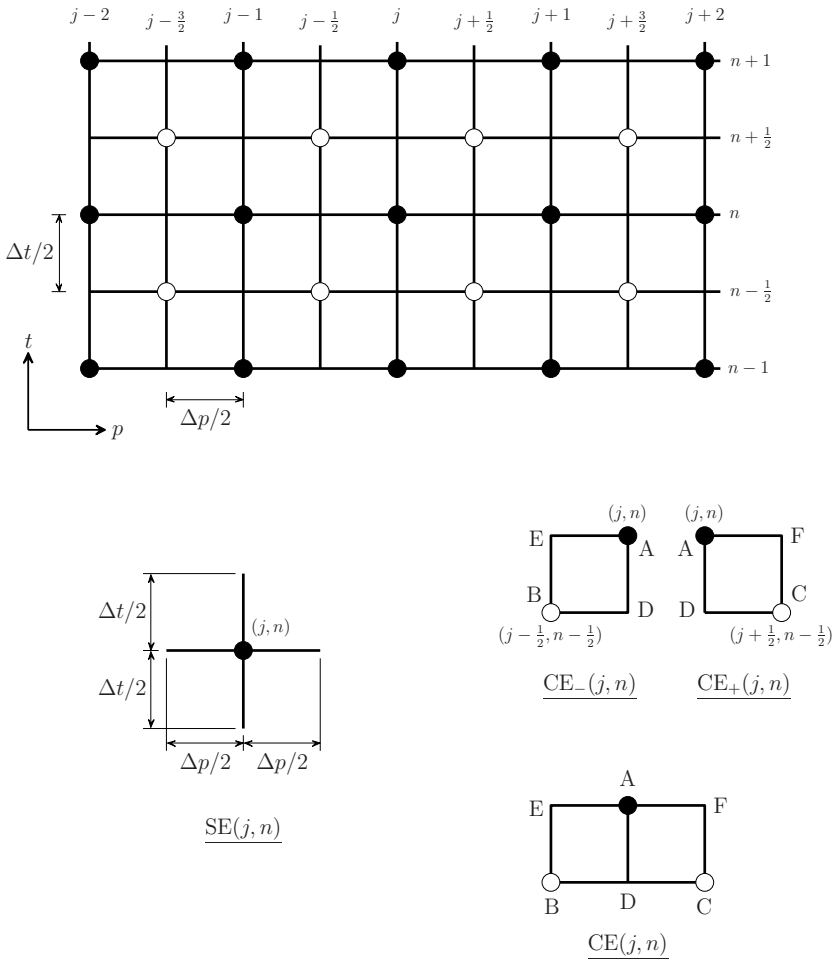

FIG. 1: Definitions of the momentum-time staggered mesh, CE, and SE in E_2.

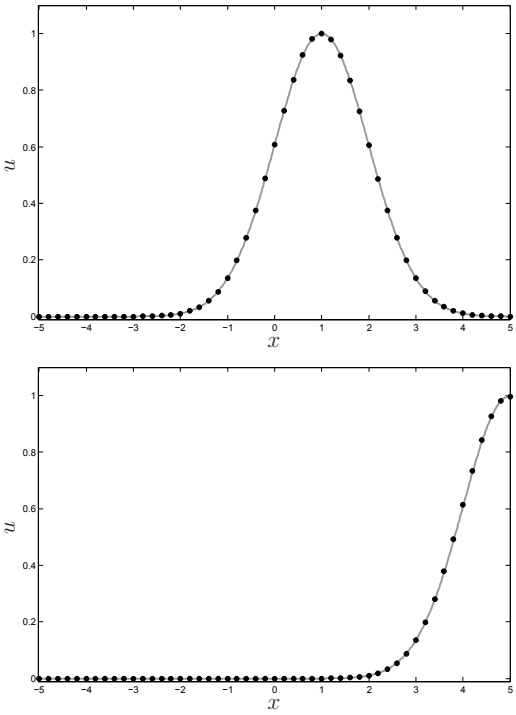

FIG. 2: Results of the coordinate space CESE a-scheme at $t = 1$ and 5 obtained with $x \in [-5, 5]$. Notice that the wave u will flow out the boundary at sufficient long time. Dots : numerical results. Solid line : exact solution.

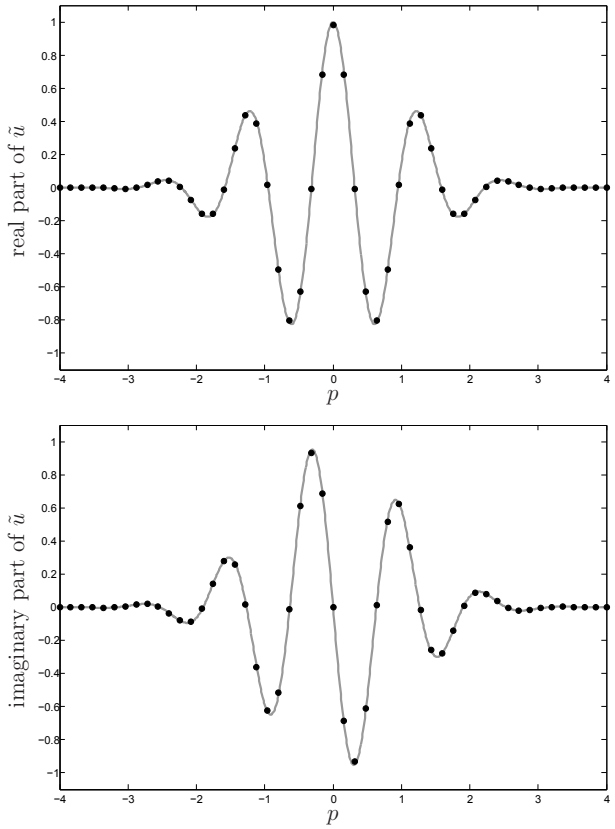

FIG. 3: Computational results $\tilde{u}$ at $t = 5$ by the p-CESE method. Data obtained with $p \in [-5, 5]$, $\Delta p = 0.16$, and $\Delta t = 0.08$. Dots : numerical results. Solid line : exact solution.

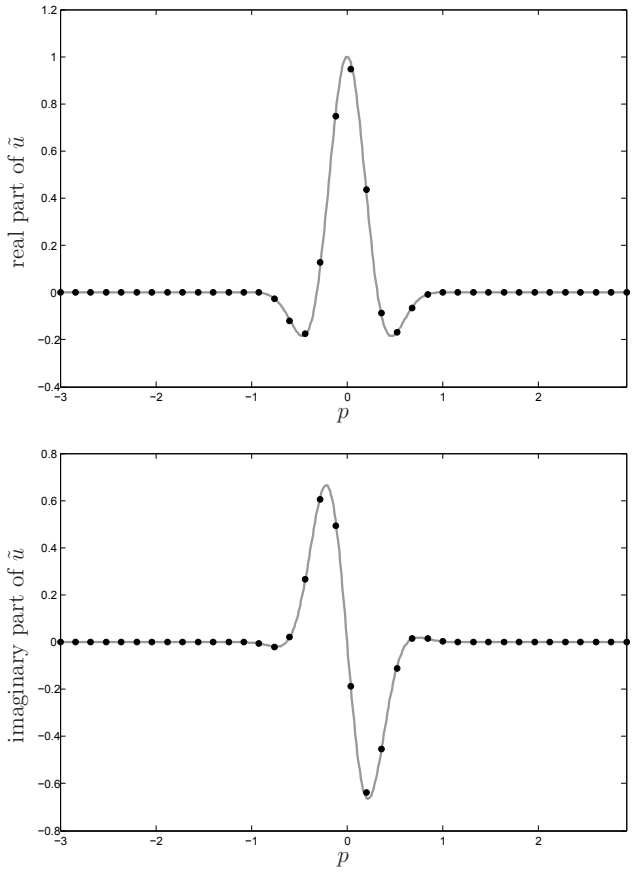

FIG. 4: Results of $\tilde{u}$ at $t = 5$ obtained with $p \in [-5, 5]$ at $\Delta p = 0.16$, and $\Delta t = 0.16$. Dots : numerical results. Solid line : exact solution.

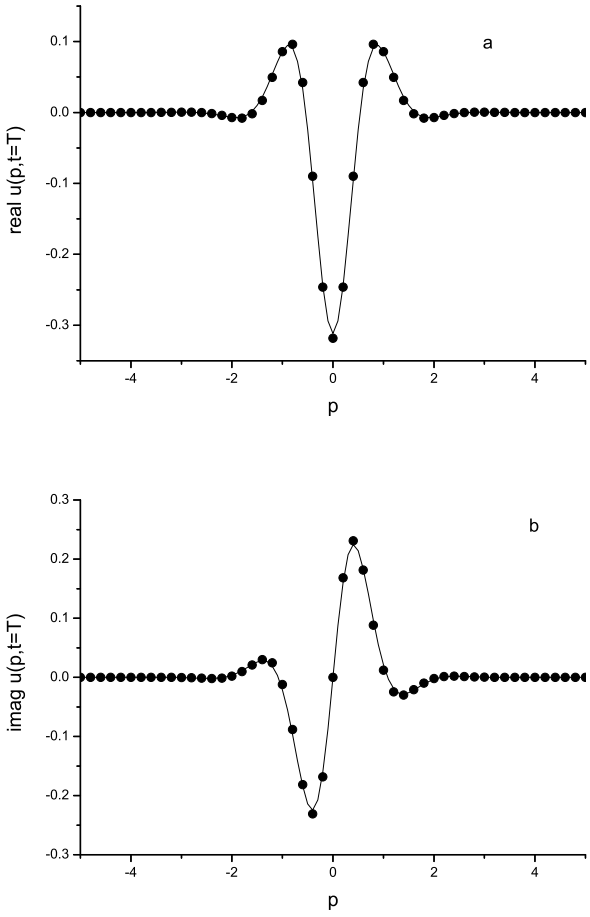

FIG. 5: Results of the real and imaginary part of KdV solution at $t = 5$ obtained with $p \in [-5, 5]$ and $\Delta t = 0.01$. Solid line : analytical solution, dots : numerical results.

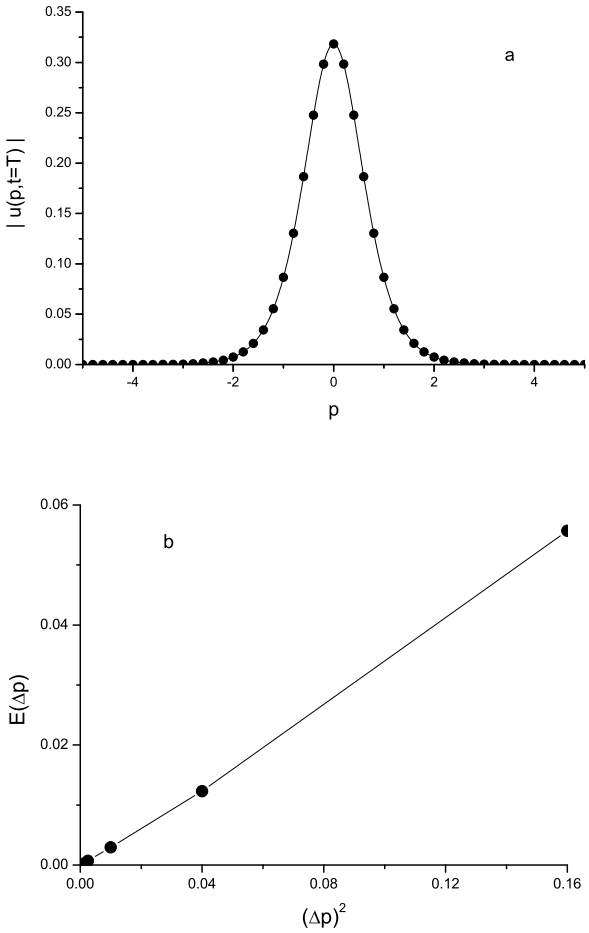

FIG. 6: a. Results of the magnitude of KdV solution at $t = 5$ obtained with $p \in [-5, 5]$ and $\Delta t = 0.01$. Solid line : exact solution, dots : numerical results. b. Error as function of square of grid size Δp. It shows $\sim O(\Delta p)^2$ behavior.

Adaptive mesh refinement for elliptic interface problems using the non-conforming immerse finite element method

Chin-Tien Wu, * Zhilin Li † Ming-Chih Lai, ‡

October 30, 2009

Abstract

In this paper, an adaptive mesh refinement technique is developted and analyzed for the non-conforming immersed finite element (IFE) method proposed in [25]. The IFE method was developed for solving the second order elliptic boundary value problem with interfaces across which the coefficient may be discontinuous. The IFE method was based on a triangulation that does not need to fit the interface. One of the key ideas of IFE method is to modify the basis functions so that the natural jump conditions are satisfied across the interface. The IFE method has shown to be order of $O(h^2)$ and $O(h)$ in L^2 norm and H^1 norm, respectively. In order to develop the adaptive mesh refinement technique, additional priori and posterior error estimations are derived in this paper. Our new a priori error estimation shows that the generic constant is only linearly proportional to ratio of the diffusive coefficients β^- and β^+, which improves the corresponding result in [25].

*Corresponding author. Department of Applied Mathematics, National Chiao-Tung University, 1001, Ta Hsueh Road, Hsinchu 300, Taiwan. ctw@math.nctu.edu.tw

†Center for Research in Scientific Computation & Department of Mathematics, North Carolina State University, Raleigh, NC. 27695-8205.

‡Center of mathematical modeling and Scientific computing, National Chiao-Tung University, 1001, Ta Hsueh Road, Hsinchu 300, Taiwan.

We also show that a posteriori error estimate similar to the one obtained by Bernardi and Verfürth [4] holds for the IFE solutions. Numerical examples support our theoretical results and show that the adaptive mesh refinement strategy is effective for the IFE approximation.

1 Introduction

The main purpose of this paper is to develop adaptive mesh refinement techniques for the immersed finite element (IFE) method proposed in [25]. Along this line, we also discuss the a priori and a posteriori error estimation for the immersed finite element method. The IFE method was developed for the following interface problem:

$$\begin{aligned} -\nabla \cdot (\beta \nabla u) &= f, \qquad (x,y) \in \Omega \\ u\mid_{\partial\Omega} &= g, \end{aligned} \tag{1}$$

together with the natural jump conditions on the interface $\tilde{\Gamma}$:

$$[u]\mid_{\tilde{\Gamma}} = 0, \tag{2}$$

$$[\beta u_n]\mid_{\tilde{\Gamma}} = 0. \tag{3}$$

Here, see the sketch in Fig.1, $\Omega \subset \mathbb{R}^2$ is a convex polygonal domain, the interface $\tilde{\Gamma}$ is a curve separating Ω into two sub-domains Ω^-, Ω^+ such that $\Omega = \Omega^- \cup \Omega^+ \cup \tilde{\Gamma}$, and the coefficient $\beta(x,y)$ is a piecewise constant function defined by

$$\beta(x,y) = \begin{cases} \beta^-, & (x,y) \in \Omega^-, \\ \beta^+, & (x,y) \in \Omega^+. \end{cases}$$

The interface problem considered here appears in many engineering and science applications. The immersed finite element (IFE) space was first introduced in [25], in which some preliminary analysis and numerical results are reported, and has been shown its capability on handling interface problems with nonhomogeneous interface jump conditions [with a nonzero constant value on the right hand of (2) and/or (3)] by either simply modifying the IFE space or reducing the interface problem to a new problem with homogeneous interface jump conditions

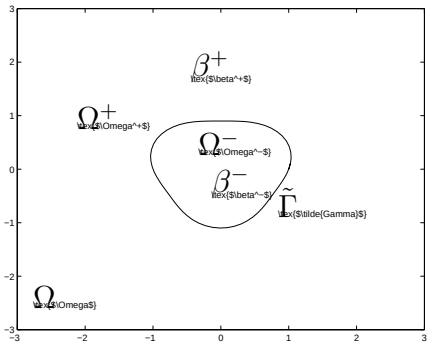

Figure 1: A rectangular domain $\Omega = \Omega^+ \cup \Omega^-$ with an immersed interface $\tilde{\Gamma}$. The coefficients $\beta(\mathbf{x})$ may have a jump across the interface.

via the usual homogenization technique based on a change of variable [23]. Some related work can be found in [**?**, 18, 19, 26].

The basic idea of the immersed finite elements is to form a partition $\Im_h$ independent of interface $\tilde{\Gamma}$ so that partitions with simple regular structures can be used to solve an interface problem with a rather complicated or varying interface. Obviously, triangles in a partition can be separated into two classes:

• Non-interface triangles: The interface $\tilde{\Gamma}$ either does not intersect with this triangle, or it intersects with this triangle but does not separate its interior into two nontrivial subsets.

• Interface triangles: The interface $\tilde{\Gamma}$ cuts through its interior.

In a non-interface triangle, the standard linear polynomials is employed as local basis functions. However, in an interface triangle, a piecewise linear polynomial is defined in the two subsets formed by the interface in a way that the functions satisfy the natural jump conditions (either exactly or approximately) on the interface and retain specified values at the vertices of the interface triangle. The immersed finite element space defined over the whole domain Ω can then be constructed through the standard finite element assembling procedure. We refer the readers to [**?**, 9–11, 14, 17, 22, 24] for more background materials about immersed interface and immersed finite element methods as well as their applications.

Without loss of generality, we assume that the triangles in the partition have the following features:

(H_1): If $\tilde{\Gamma}$ meets one edge of a triangle at more than two points, then the edge is part of $\tilde{\Gamma}$.

(H_2): If $\tilde{\Gamma}$ meets a triangle at two points, then these two points must be on different edges for this triangle.

In order to obtain error estimates, we assume that the underlying mesh is fine enough such that the interface can be approximated by a line segment with a small perturbation in a magnitude of $O(h^2)$. Furthermore, the source function f and the interface $\tilde{\Gamma}$ are assumed to be smooth enough such that the weak solution of the problem (1) can be approximated by a piecewise C^2 function. These requirements lead to our third hypothesis:

(H_3): The segment of the interface $\tilde{\Gamma}$ in a triangle $T \in \Im_h$ is defined by a piecewise C^2 function and the function space $C^2(T)$ is dense in $H^2(T)$.

It is well known that the standard finite element method (FE) with linear finite elements can be used to solve such elliptic interface problems [see [3, 5, 6] and the references therein]. However, in order to achieve the optimal $O(h^2)$ accuracy in the numerical solutions, an interface fitted grid is needed. In applications with nontrivial interfaces or the time-varying interfaces, this restriction prevents the Galerkin method with linear finite elements from working efficiently since mesh moving or re-meshing is required. On the other hand, although the mesh moving and re-meshing may produce extra technical difficulties and computation overhead for the standard FE method, the standard FE method has a great advantage on increasing the accuracy of the numerical solutions at low cost through the adaptive mesh refinement process. In the adaptive mesh refinement process, first an error indicator η_T used to pin point the locations with large error is computed on each element in a given triangulation. Second, the elements in which the error indicator has large value are marked for refinement according to a given marking strategy. A heuristic marking strategy is the maximum marking strategy where an element T^* will be marked for refinement if $\eta_{T^*} > \theta \max_{T\in\Im_h} \eta_T$, with a prescribed threshold $0 \leq \theta \leq 1$. Some other marking strategies can also be seen in [13]. Finally, the marked triangles are divided into sub-triangles by rules such as the regular

refinement algorithm or the longest side bisection algorithm [15] [16]. An approximate solution is then computed on the refined mesh. The above procedure can be repeatedly applied until the accuracy of the approximated solution is satisfied. The theoretical foundation of the mesh refinement strategy is based on the a posteriori error estimation proposed by Babuška and Rheinboldt [1] and further developed by many researchers such as Zienkiewicz [27], Bank and Weiser [2], and Verfürth [20, 21]. The convergence of the adaptive mesh refinement process has been shown by Morin, Nochetto and Siebert [12].

It has been shown that the IFE interpolation errors on a uniform fixed (such as Cartesian) partition is of the order of $O(h)$ in the H^1 norm and of the order of $O(h^2)$ in the L^∞ and L^2 norms under the hypothesis (H_1), (H_2) and (H_3) [26]. In this work, we obtain the same order of the error estimations and further show that the generic constants in these estimations are linearly proportional to the ratio $\max\left\{\rho, \frac{1}{\rho}\right\}$ of the diffusion coefficients, here $\rho = \frac{\beta^-}{\beta^+}$. The a posteriori estimations of the finite element solutions mentioned above are obtained mostly on fitted grids. Recently, A. Hansbo and P. Hansbo propose an unfitted finite element method for the elliptic interface problem. The same order of a priori error estimations is obtained and an a posteriori estimator is proposed [8]. Here, we also derive an a posteriori error estimation for the IFE method based on the methodology developed by Verfürth [4]. Our numerical results support the effectiveness of the proposed a posteriori error estimation.

This paper is organized as follows. In section 2, we show the existence and uniqueness of the element IFE basis function and derive some auxiliary inequalities that are needed for the error estimation in section 3. We derive the a priori error estimations and the a posteriori error estimation in section 3 and present our numerical results in section 4. Finally, we draw our conclusions in section 5.

2 Review of the immersed finite element space

First we present a brief review of the immersed finite element space and the construction of the basis functions.

Given a regular mesh $\Im_h$ on the domain Ω, let T be an interface triangle in

$\Im_h$ with vertices A, B and C where the interface passes through the interior of T and intersect with the edges of T at points D and E. Let $\tilde{\Gamma}_T = \tilde{\Gamma} \cap T$. In the immersed finite element method, the interface $\tilde{\Gamma}_T$ is commonly approximated by the line segment $\overline{DE}$, denoted by Γ_T. The formulation of the immersed finite element method follows the idea that similar to the Hsieh-Clough-Tocher macro element [7] in which the piecewise polynomial in each element is required to satisfy certain constrains to ensure the C^1-continuity on the whole domain. The immersed finite element space on a triangle T, denoted by $S_h^I(T)$, is the linear space of all piecewise linear functions that satisfy the continuity condition $[\phi]_{\Gamma_T} = 0$ and the homogeneous flux jump condition $[\beta \partial_n \phi]_{\Gamma_T} = 0$ on the approximate interface Γ_T. Assume the element basis functions on the reference triangle have the following form:

$$\phi^+ = a_0 + a_1 x + a_2 y \ \text{ for } (x, y) \in T^+$$
$$\phi^- = b_0 + b_1 x + b_2 y \ \text{ for } (x, y) \in T^-.$$

It has been shown that the coefficients a_i and b_i, $i = 1 \cdots 3$, can be determined uniquely. In [25], the continuity condition $[\phi]_{\Gamma_T} = 0$ is satisfied by enforcing the continuity on the intersection points D and E, i.e., $\phi^+(D) = \phi^-(D)$ and $\phi^+(E) = \phi^-(E)$. In this work, we replace the condition $\phi^+(E) = \phi^-(E)$ by $\vec{t} \cdot \nabla \phi^+ = \vec{t} \cdot \nabla \phi^-$, here $\vec{t}$ is the unit tangent of the approximated interface Γ_T. The existence and uniqueness of the immersed finite element basis functions are reassured in the following theorem. The interpolation errors in the L^∞, L^2 and H^1 norms will be estimated in the next section.

Theorem 2.1 *Let T denote a triangle with vertices (x_i, y_i), $i = 1 \cdots 3$ in a given uniform mesh, the associated IFE basis functions $\phi \in S_h^I(T)$ consisting of ϕ^+ and ϕ^- on the reference triangle are uniquely determined by the nodal values $\phi(x_i, y_i)$, $i = 1 \cdots 3$.*

Proof: Let Φ be the affine transformation that maps the reference triangle to the triangle T via $\Phi(0, 0) = (x_1, y_1)$, $\Phi(1, 0) = (x_2, y_2)$ and $\Phi(0, 1) = (x_3, y_3)$. Let $\phi(x_i, y_i) = \phi_i$, $i = 1 \cdots 3$. From the nodal values and the continuity at

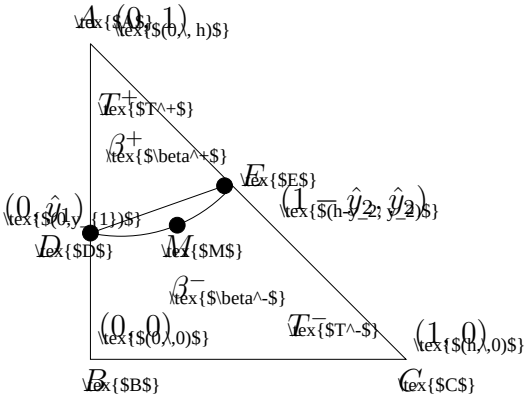

Figure 2: A typical triangle element with an interface cutting through. The arc DME is part of the interface curve $\tilde{\Gamma}$ which is approximated by the line segment $\overline{DE}$. In this picture, T is the triangle $\triangle ABC$, $T^+ = \triangle ADE$, $T^- = T - T^+$, and T^* is the region enclosed by the $\overline{DE}$ and $\tilde{\Gamma}$.

node D, we have

$$\begin{aligned} \phi_3 &= \phi^+(0,1) = a_0 + a_2 \Rightarrow a_0 = \phi_3 - a_2 && (4)\\ \phi_1 &= \phi^-(0,0) = b_0 && (5)\\ \phi_2 &= \phi^-(1,0) = b_0 + b_1 \Rightarrow b_1 = \phi_2 - \phi_1 && (6)\\ a_0 + a_2\hat{y}_1 &= b_0 + b_2\hat{y}_1. && (7) \end{aligned}$$

Plugging equations (4) and (5) into equation (7) implies

$$(-1 + \hat{y}_1)a_2 - \hat{y}_1 b_2 = \phi_1 - \phi_3. \tag{8}$$

Moreover, from the flux continuity condition and the continuity of the solution along the tangential direction of the interface, we have

$$\begin{cases} \vec{n}(\Phi^{-1})^T \nabla\phi^+ = \rho\vec{n}(\Phi^{-1})^T \nabla\phi^- \\ \vec{t}(\Phi^{-1})^T \nabla\phi^+ = \vec{t}(\Phi^{-1})^T \nabla\phi^-, \end{cases} \tag{9}$$

where $n = (n_1, n_2)$ and $t = (-n_2, n_1)$ are the normal and tangent vectors of the interface respectively, and $\rho = \frac{\beta^-}{\beta^+}$. Let $(m_1, m_2) = \vec{n}(\Phi^{-1})^T$ and $(m_3, m_4) = \vec{t}(\Phi^{-1})^T$. The two equations in (9) can be rewritten as following:

$$\begin{aligned} m_1 a_1 + m_2 a_2 - \rho m_2 b_2 &= -\rho m_1 \phi_1 + \rho m_1 \phi_2 && (10)\\ m_3 a_1 + m_4 a_2 &= m_3(\phi_2 - \phi_1) + m_4 b_2. && (11) \end{aligned}$$

Plugging (8) into (10) and (11) and writing the resulted equations in the matrix form, we have

$$\begin{aligned}
&\begin{bmatrix} m_1\hat{y}_1 & m_2(\hat{y}_1+\rho(1-\hat{y}_1)) \\ m_3\hat{y}_1 & m_4 \end{bmatrix}\begin{bmatrix} a_1 \\ a_2 \end{bmatrix} \\
&= \begin{bmatrix} (-\rho m_2-\rho m_1\hat{y}_1) & \rho m_1\hat{y}_1 & \rho m_2 \\ -m_4-m_3\hat{y}_1 & m_3\hat{y}_1 & m_4 \end{bmatrix}\begin{bmatrix} \phi_1 \\ \phi_2 \\ \phi_3 \end{bmatrix} \qquad (12)\\
&= \begin{bmatrix} \rho m_1\hat{y}_1 & \rho m_2 \\ m_3\hat{y}_1 & m_4 \end{bmatrix}\begin{bmatrix} \phi_2-\phi_1 \\ \phi_3-\phi_1 \end{bmatrix}.
\end{aligned}$$

To prove the theorem, we only need to show the metric

$$A = \begin{bmatrix} m_1\hat{y}_1 & m_2(\hat{y}_1+\rho(1-\hat{y}_1)) \\ m_3\hat{y}_1 & m_4 \end{bmatrix}$$

is non-singular. Let $\rho^* = \hat{y}_1 + \rho(1-\hat{y}_1)$. We can see clearly that $\rho^* \geq 1$ when $\rho \geq 1$ and $0 \leq \rho^* \leq 1$ when $\rho \leq 1$. Since $m_1m_4 - m_2m_3 = det(\Phi) > 0$, $m_2m_3 < 0$ and $m_1m_4 > 0$, we have

$$det(A) = \hat{y}_1((m_1m_4 - m_2m_3) - (\rho^*-1)m_2m_3) > 0, \text{ if } \rho \geq 1 \qquad (13)$$

and

$$det(A) = m_1m_4(1-\rho^*)\hat{y}_1 + \rho^*\hat{y}_1(m_1m_4 - m_2m_3) > 0, \text{ if } 0 < \rho < 1. \qquad (14)$$

Now from (13) and (14), we can conclude the matrix A is nonsingular and the theorem holds. □

Remark 2.2 *We can further estimate*

$$\begin{aligned}
det(A) &= \hat{y}_1(h^{-2} + (\rho^*-1)n_y^2) = h^{-2}(\hat{y}_1\rho^*) \\
&= h^{-2}(\hat{y}_1(\hat{y}_1+\rho(1-\hat{y}_1))) > \min\{1,\rho\}h^{-2}\hat{y}_1, \ \textit{for } \rho > 1, \textit{ and} \\
det(A) &= h^{-2}\hat{y}_1 > \hat{y}_1h^{-2}\min\{1,\rho\}, \ \textit{for } 0 \leq \rho \leq 1,
\end{aligned}$$

from the equations (13) and (14), respectively. Therefore, the following estimation of $det(A)$ *holds*

$$det(A) \geq \hat{y}_1h^{-2}\min\{1,\rho\}. \qquad (15)$$

Moreover, Let $\Delta\phi_1 = \phi_2 - \phi_1$, $\Delta\phi_2 = \phi_3 - \phi_1$, *and* $B = \begin{bmatrix} \rho m_1 \hat{y}_1 & \rho m_2 \\ m_3 \hat{y}_1 & m_4 \end{bmatrix}$. *The equation (12) implies*

$$\begin{aligned} \begin{bmatrix} a_1 - \Delta\phi_1 \\ a_2 - \Delta\phi_2 \end{bmatrix} &= A^{-1}(B - A) \begin{bmatrix} \Delta\phi_1 \\ \Delta\phi_2 \end{bmatrix} \\ &= \frac{\hat{y}_1(\rho - 1)}{\det(A)} \begin{bmatrix} m_2 m_4 & m_2 m_4 \\ -\hat{y}_1 m_2 m_3 & -\hat{y}_1 m_2 m_3 \end{bmatrix} \begin{bmatrix} \Delta\phi_1 \\ \Delta\phi_2 \end{bmatrix}. \end{aligned} \tag{16}$$

Also, from the equations (6), (8), and (16), we have

$$\begin{aligned} \begin{bmatrix} b_1 - \Delta\phi_1 \\ b_2 - \Delta\phi_2 \end{bmatrix} &= \begin{bmatrix} 0 \\ \frac{\hat{y}_1 - 1}{\hat{y}_1}(a_2 - \Delta\phi_2) \end{bmatrix} \\ &= \frac{\hat{y}_1(\hat{y}_1 - 1)(\rho - 1)}{\det(A)} \begin{bmatrix} 0 & 0 \\ -m_2 m_3 & -m_2 m_3 \end{bmatrix} \begin{bmatrix} \Delta\phi_1 \\ \Delta\phi_2 \end{bmatrix} \end{aligned} \tag{17}$$

By applying the estimation (15) to the equations (16) and (17), we can easily show that the following inequalities hold:

$$\begin{aligned} \left\| \begin{pmatrix} a_2 - \Delta\phi_1 \\ a_3 - \Delta\phi_2 \end{pmatrix} \right\|_\infty &\le c^+ \max\{\rho, \frac{1}{\rho}\} \left\| \begin{pmatrix} \Delta\phi_1 \\ \Delta\phi_2 \end{pmatrix} \right\|_\infty, \\ \left\| \begin{pmatrix} b_2 - \Delta\phi_1 \\ b_3 - \Delta\phi_2 \end{pmatrix} \right\|_\infty &\le c^- \max\{\rho, \frac{1}{\rho}\} \left\| \begin{pmatrix} \Delta\phi_1 \\ \Delta\phi_2 \end{pmatrix} \right\|_\infty, \end{aligned} \tag{18}$$

where c^+ *and* c^- *are constants independent with* ρ.

3 The priori and posteriori error estimations

In this section, we define the IFE solution of the interface problem (1) and derive the priori and posteriori error estimations of the IFE solution. We first introduce some notations in the following:

- Let $\Im_h$ denote the regular mesh that satisfies the usual admissibility and the shape regularity. Let $\breve{\Im}_h$ be the set of elements intersect with the interface,

and $\overset{\circ}{\Im}_h = \Im_h \setminus \breve{\Im}_h$. For $\tau \in \Im_h$, let $\partial\tau$ denote the set of boundary segments of the element τ and $\mathcal{E}_h = \cup_{\tau\in\Im_h}\partial\tau$. Let $\breve{\mathcal{E}}_h$ be the set of edges intersect with the interface and $\overset{\circ}{\mathcal{E}}_h = \mathcal{E}_h \setminus \breve{\mathcal{E}}_h$. Moreover, N_h = the set of all vertices in $\Im_h$, N_τ = vertices of an element τ and N_e = vertices of an edge $e \in \mathcal{E}_h$. Also, for any element $\tau \in \Im_h$, edge $e \in \mathcal{E}$ and node $z \in N_h$, let

$$\omega_\tau = \bigcup_{\tau'\cap\tau\in\partial\tau} \tau',\ \tilde{\omega}_\tau = \bigcup_{\tau'\cap\tau\neq\emptyset} \tau',\ \omega_e = \bigcup_{N_\tau\cap N_e\neq\emptyset'} \tau',\ \omega_z = \bigcup_{z\in\tau'} \tau'$$

- We denote by H^0 and H^k, the usual Lebesgue L^2-integrable space and the Sobolev spaces equipped with the standard norms $\|f\|_k$ for $f \in H^k$, $k = 0\cdots 2$. The notations $\|f\|_{k,\Omega_0}$, $k = 0\cdots 2$, and $\|f\|_{\beta,\Omega_0}$ denote the usual Sobolev norms and the energy norm of f on a sub-domain $\Omega_0 \subset \Omega$. The piecewise linear polynomial space on a sub-domain Ω_0 is denoted by $S_h(\Omega_0)$. The immersed finite element space on the domain Ω, is denoted by $S_h^I(\Omega)$, is defined by $S_h^I(\Omega) = \{\phi \mid \phi|_\tau \in S_h^I(\tau),\ \text{for all } \tau \in \Im_h,\ \text{and } \phi|_\tau(z) = \phi|_{\tau'}(z),\ \text{for } z \in N_\tau \cap N_{\tau'}\}$. The notation $S_{h,0}^I(\Omega)$ denote the sub-space in $S_h^I(\Omega)$ with homogeneous boundary condition, $\{\phi \in S_h^I(\Omega) \mid \phi|_{\partial\Omega} = 0\}$.

- For each vertex $z \in N_h$, let φ_z denote the linear nodal basis function. With every element τ and every edge e, we associate the bubble functions $\psi_\tau = 27\prod_{z\in N_\tau}\varphi_z$ and $\psi_e = 4\prod_{z\in N_e}\varphi_z$. Let I_n denote the nodal interpolant, π_z denote the L^2 orthogonal projection onto the piecewise linear function space in ω_z, and I_π denote the quasi-interpolant of a function u defined as $I_\pi u = \sum_{z\in\Im_h}(\pi_z u)\varphi_z$.

For any function $\phi \in H^1(\Omega)$, the IFE interpolant of ϕ is denoted by $\phi_I \in S_h^I$ that satisfies $\varphi_z\phi_I = \phi(z)$ for all $z \in N_h$. The IFE solution of problem (1) denoted by u_h^I satisfies the standard variation formulation of (1) as following:

$$(\beta\nabla\nu\ ,\ \nabla u_h^I) = (\nu\ ,\ f),\ \text{for all } \nu \in S_{h,0}^I(\Omega),$$

where $(\cdot\ ,\ \cdot)$ is the usual inner product in the $H^0(\Omega)$. To derive the a priori error estimations of $\left\|u - u_h^I\right\|_0$ and $\left\|u - u_h^I\right\|_1$, we need to estimate the interpolation errors of $\phi - \phi_I$ for any $\phi \in H^1(\Omega) \cap C(\Omega)$, here $\phi_I \in S_h^I(T)$ denote the IFE

interpolant of ϕ. In the following theorem, we first estimate the errors of $\phi - \phi_I$ and $\nabla\phi - \nabla\phi_I$ in the L^∞ norm.

Theorem 3.1 *Let T be a triangle in a uniform mesh $\Im_h$ and the interface $\tilde{\Gamma}$ satisfies the hypothesis $(H1)$, $(H2)$ and $(H3)$. Let Γ_T denote the line segment that approximates $\tilde{\Gamma}_T$. Let ϕ be an arbitrary function in $C^2(T)$ and $\phi_I \in S_h^I(T)$ be the IFE interpolant of ϕ. The following error estimates hold.*

$$\|\nabla\phi(x,y) - \nabla\phi_I(x,y)\|_{\infty,T} \leq \begin{cases} ch\,\|D^2\phi\|_{\infty,T} & \text{when } (x,y) \in \Omega\backslash T^* \\ c\,\|D^2\phi\|_{\infty,T} & \text{when } (x,y) \in T^* \end{cases} \tag{19}$$

$$\|\phi(x,y) - \phi_I(x,y)\|_{\infty,T} \leq ch^2\left\|D^2\phi\right\|_{\infty,T}, \tag{20}$$

where $c = O(\max\{\frac{1}{\rho}, \rho\})$ and T^* is the region enclosed by $\tilde{\Gamma}_T$ and Γ_T.

Proof: First, we estimate the error of $\nabla\phi - \nabla\phi_I$ at element nodal points of the reference triangle in the following: From the Taylor expansion of ϕ, we have

$$\phi^+(\hat{x},\hat{y}) = \phi^+(0,1) + \nabla\phi^+(0,1)\begin{bmatrix} \hat{x} \\ \hat{y}-1 \end{bmatrix} + e_1 \tag{21}$$

$$\phi^-(\hat{x},\hat{y}) = \phi^-(0,0) + \nabla\phi^-(0,0)\begin{bmatrix} \hat{x} \\ \hat{y} \end{bmatrix} + e_2, \tag{22}$$

where $e_1 \leq (\hat{y}_1-1)(\|D^2\phi\|_\infty(\hat{y}_1-1)h^2)$ and $e_2 \leq \hat{y}_1\|D^2\phi\|_\infty \hat{y}_1h^2$, and $|e_2 - e_1| \leq 2\max_{v\in\{|\hat{y}_1|,|\hat{y}_1-1|\}}\{v^T\|D^2\phi\|_\infty v\}h^2$. By imposing the continuity at node D, from (21) and (22), we have

$$\begin{aligned} \phi(0,\hat{y}_1) &= \phi^+(0,1) + \phi^+_{\hat{y}}(0,1)(\hat{y}_1-1) + e_1 \\ &= \phi^-(0,0) + \phi^-_{\hat{y}}(0,0)(\hat{y}_1) + e_2. \end{aligned}$$

The above equation implies

$$(-1+\hat{y}_1)\phi^+_{\hat{y}}(0,1) - \hat{y}_1\phi^-_{\hat{y}}(0,0) = \phi_1 - \phi_3 + e_2 - e_1. \tag{23}$$

Next, from the flux continuity and tangential continuity on the interface, we have

$$\begin{aligned} m_1\phi^+_{\hat{x}} + m_2\phi^+_{\hat{y}} &= \rho(m_1\phi^-_{\hat{x}} + m_2\phi^-_{\hat{y}}) \\ m_3\phi^+_{\hat{x}} + m_4\phi^+_{\hat{y}} &= m_3\phi^-_{\hat{x}} + m_4\phi^-_{\hat{y}}. \end{aligned} \tag{24}$$

By differentiating (21) and (22), and evaluating (22) at (1,0), we have

$$\begin{cases} \phi^+_{\hat{x}}(\hat{x},\hat{y}) = \phi^+_{\hat{x}}(0,1) + e_3 \\ \phi^+_{\hat{y}}(\hat{x},\hat{y}) = \phi^+_{\hat{y}}(0,1) + e_4 \\ \phi^-_{\hat{y}}(\hat{x},\hat{y}) = \phi^-_{\hat{y}}(0,0) + e_5 \\ \phi^-_{\hat{x}}(\hat{x},\hat{y}) = \phi^-_{\hat{x}}(0,0) + e_6, \end{cases} \tag{25}$$

here $e_i = o(h)$, $i = 3 \cdots 6$, and

$$\phi^-_{\hat{x}}(0,0) = \phi^-(1,0) - \phi^-(0,0) + e_2. \tag{26}$$

Now plugging (23), (25) and (26) into (24), the equation (24) can now be rewritten in a matrix form as following:

$$\begin{aligned} &\begin{bmatrix} m_1\hat{y}_1 & m_2(\hat{y}_1 + \rho(1-\hat{y}_1)) \\ m_3\hat{y}_1 & m_4 \end{bmatrix} \begin{bmatrix} \phi^+_{\hat{x}}(0,1) \\ \phi^+_{\hat{x}}(0,1) \end{bmatrix} \\ &= \begin{bmatrix} -\rho m_2 - \rho m_1\hat{y}_1 & \rho m_1\hat{y}_1 & \rho m_2 \\ -m_4 - m_3\hat{y}_1 & m_3\hat{y}_1 & m_4 \end{bmatrix} \begin{bmatrix} \phi_1 \\ \phi_2 \\ \phi_3 \end{bmatrix} + \hat{y}_1 \begin{bmatrix} \tilde{e}_1 \\ \tilde{e}_2, \end{bmatrix} \end{aligned} \tag{27}$$

where $\tilde{e}_i = o(1)$, for $i = 1, 2$. Let $\delta^+_x = (\phi^+_I)_{\hat{x}} - \phi^+_{\hat{x}}$, $\delta^+_y = (\phi^+_I)_{\hat{y}} - \phi^+_{\hat{y}}$, $\delta^-_x = (\phi^-_I)_{\hat{x}} - \phi^-_{\hat{x}}$ and $\delta^-_y = (\phi^-_I)_{\hat{y}} - \phi^-_{\hat{y}}$. Recall that $a_1 = (\phi^+_I)_{\hat{x}}$, $a_2 = (\phi^+_I)_{\hat{y}}$, $b_1 = (\phi^-_I)_{\hat{x}}$, $b_2 = (\phi^-_I)_{\hat{y}}$, and

$$A = \begin{bmatrix} m_1\hat{y}_1 & m_2(\hat{y}_1 + \rho(1-\hat{y}_1)) \\ m_3\hat{y}_1 & m_4 \end{bmatrix}$$

Subtracting (12) from (27) leads to the following equation

$$A \begin{bmatrix} \delta^+_x(0,1) \\ \delta^+_y(0,1) \end{bmatrix} = \hat{y}_1 \begin{bmatrix} \tilde{e}_1 \\ \tilde{e}_2. \end{bmatrix} \tag{28}$$

By applying the lower bound of $det(A)$ in Remark 2.2 on the solution of the equation (28), we have

$$
\begin{aligned}
|\delta_x^+(0,1)| &= |\frac{\hat{y}_1(m_4\tilde{e}_1 - (\hat{y}_1 + \rho(1-\hat{y}_1))m_2\tilde{e}_2)}{det(A)}| \\
&< (|m_4\tilde{e}_1| + (\hat{y}_1 + \rho(1-\hat{y}_1))|m_2\tilde{e}_2|)\frac{h^2}{\min\{1,\rho\}} \\
&< c\frac{\max\{1,\rho\}}{\min\{1,\rho\}}h < c\cdot\max\{\rho,\frac{1}{\rho}\}h \qquad (29) \\
|\delta_y^+(0,1)| &= |\frac{\hat{y}_1(m_3\hat{y}_1\tilde{e}_1 + m_1\hat{y}_1\tilde{e}_2)}{det(A)}| \\
&< \hat{y}_1(|m_3\tilde{e}_1| + |m_1\tilde{e}_2|)\frac{h^2}{\min\{1,\rho\}} \\
&< c\hat{y}_1\cdot\max\{\rho,\frac{1}{\rho}\}h \qquad (30)
\end{aligned}
$$

Similarly, by subtracting (6) from (26) and subtracting (8) from (23), we have the following inequalities

$$
\begin{aligned}
|\delta_x^-(0,0)| &< ch^2 \qquad (31) \\
|\delta_y^-(0,0)| &< |\frac{(-1+\hat{y}_1)}{\hat{y}_1}\delta_y^+(0,1)| + |\frac{e_1-e_2}{\hat{y}_1}| \\
&< c\max\{\rho,\frac{1}{\rho}\}h + o(h^2). \qquad (32)
\end{aligned}
$$

As a result of (25), (29), (30)-(32), the following error estimates hold

$$
\begin{aligned}
|(\phi_{\hat{x}}^+ - (\phi_I^+)_{\hat{x}})(\hat{x},\hat{y}))| &< |\phi_{\hat{x}}^+(\hat{x},\hat{y}) - \phi_{\hat{x}}^+(0,1)| + |(\phi_{\hat{x}}^+ - (\phi_I^+)_{\hat{x}})(0,1)| < c_1 h \\
|(\phi_{\hat{y}}^+ - (\phi_I^+)_{\hat{y}})(\hat{x},\hat{y}))| &< |\phi_{\hat{y}}^+(\hat{x},\hat{y}) - \phi_{\hat{y}}^+(0,1)| + |(\phi_{\hat{y}}^+ - (\phi_I^+)_{\hat{y}})(0,1)| < c_2 h,
\end{aligned} \qquad (33)
$$

for $(\hat{x},\hat{y}) \in T^+ \setminus T^*$, and

$$
\begin{aligned}
|(\phi_{\hat{x}}^- - (\phi_I^-)_{\hat{x}})(\hat{x},\hat{y})| &\leq |\phi_{\hat{x}}^-(\hat{x},\hat{y}) - \phi_{\hat{x}}^-(0,0)| + |(\phi_{\hat{x}}^- - (\phi_I^-)_{\hat{x}})(0,0)| < c_3 h \\
|(\phi_{\hat{y}}^- - (\phi_I^-)_{\hat{y}})(\hat{x},\hat{y})| &\leq |\phi_{\hat{y}}^-(\hat{x},\hat{y}) - \phi_{\hat{y}}^-(0,0)| + |(\phi_{\hat{y}}^- - (\phi_I^-)_{\hat{y}})(0,0)| < c_4 h
\end{aligned} \qquad (34)
$$

for $(\hat{x},\hat{y}) \in T^- \setminus T^*$, where $c_i = o\left(\max\{\rho, 1/\rho\}\left\|D^2u\right\|_\infty\right)$, for $i = \cdots 4$.

Finally, for $(\hat{x},\hat{y}) \in T^*$, we have

$$\nabla\phi(\hat{x},\hat{y}) - \nabla\phi_I(\hat{x},\hat{y}) = \nabla\phi(\bar{x},\bar{y}) - \nabla\phi_I(\bar{x},\bar{y}) + \delta_1 + \delta_2,$$

for some $(\bar{x},\bar{y}) \in T^-$, where $\delta_1 = \nabla(\phi(\hat{x},\hat{y}) - \phi(\bar{x},\bar{y}))$ and $\delta_2 = \nabla(\phi_I^+ - \phi_I^-)(\hat{x},\hat{y})$. Since $\|\nabla(\phi-\phi_I)(\bar{x},\bar{y})\| < c_4 h$ and $\|\delta_1\| < c_5 h$, from (34) and Taylor formula, where c_5 depends on $\|D^2\phi\|_\infty$, we only need to estimate δ_2 to control the error $|\nabla\phi(\hat{x},\hat{y}) - \nabla\phi_I(\hat{x},\hat{y})|$.

Recall that from the flux continuity and tangential continuity, we have

$$\begin{bmatrix} m_1 & m_2 \\ m_3 & m_4 \end{bmatrix} \begin{bmatrix} a_1 \\ a_2 \end{bmatrix} = \begin{bmatrix} \rho m_1 & \rho m_2 \\ m_3 & m_4 \end{bmatrix} \begin{bmatrix} b_1 \\ b_2 \end{bmatrix}.$$

We can clearly see that,

$$\begin{aligned} \|\delta_2\| &= \|\nabla(\phi_I^- - \phi_I^+)(\hat{x},\hat{y})\| = \left\| \begin{bmatrix} a_1 - b_1 \\ a_2 - b_2 \end{bmatrix} \right\| \\ &\le \left\| \left(\begin{bmatrix} \rho m_1 & \rho m_2 \\ m_3 & m_4 \end{bmatrix}^{-1} \begin{bmatrix} m_1 & m_2 \\ m_3 & m_4 \end{bmatrix} - I \right) \right\| \left\| \begin{bmatrix} a_1 \\ a_2 \end{bmatrix} \right\|. \end{aligned} \tag{35}$$

From (33) and the assumption $\phi \in C^2(T)$, we have

$$\left\| \begin{bmatrix} a_1 \\ a_2 \end{bmatrix} \right\| \le \left\| \begin{bmatrix} a_1 \\ a_2 \end{bmatrix} - \begin{bmatrix} {\phi_{\hat{x}}}^+ \\ {\phi_{\hat{y}}}^+ \end{bmatrix} \right\| + \left\| \begin{bmatrix} {\phi_{\hat{x}}}^+ \\ {\phi_{\hat{y}}}^+ \end{bmatrix} \right\| < c_6, \tag{36}$$

for some constant c_6 depends on $\|D^2\phi\|_\infty$. Moreover, since

$$\begin{aligned} \left\| \begin{bmatrix} \rho m_1 & \rho m_2 \\ m_3 & m_4 \end{bmatrix}^{-1} \left(\begin{bmatrix} m_1 & m_2 \\ m_3 & m_4 \end{bmatrix} - I \right) \right\| &\le c_7 \left| \frac{1-\rho}{\rho h^{-2}} \right| \left\| \begin{bmatrix} m_1 m_4 & m_2 m_4 \\ -m_1 m_3 & -m_2 m_3 \end{bmatrix} \right\| \\ &\le c_7 \left| \frac{1-\rho}{\rho} \right| \le c_7 \max\{\frac{1}{\rho}, \rho\}, \end{aligned} \tag{37}$$

for some constant c_7, because m_1, m_2, m_3 and m_4 are $O(h^{-1})$. From (35), (36) and (37), we can conclude that

$$\|\nabla\phi(\hat{x},\hat{y}) - \nabla\phi_I(\hat{x},\hat{y})\|_\infty < c_8 \max\{\frac{1}{\rho}, \rho\} \text{ for } (\hat{x},\hat{y}) \in T^*, \tag{38}$$

where the constant c_8 depends on $\|D^2\phi\|_\infty$. Finally, from (33), (34) and (38), we can conclude the inequality (19) holds. The inequality (20) can then be proved by following the same argument as shown in the Theorem 2.3 [25]. □

With the help of the above theorem, we can easily obtain the traditional interpolation error estimation in the L^2-norm and H^1-norm.

Theorem 3.2 *The following interpolation error estimates hold. For function $\phi \in H^2(\Omega)$, if ϕ is a piecewise C^2 function on any interface element τ, for all $\tau \in \overset{\circ}{\Im}_h$, then there exist constants c_0 and c_1 such that*

$$\|\phi - \phi_I\|_0 < c_0 h^2 \|\phi\|_2 \quad (39)$$

$$\|\phi - \phi_I\|_1 < c_1 h \|\phi\|_2 , \quad (40)$$

where c_0 and c_1 are $O(\max\{1/\rho, \rho\})$.

Proof: We first prove inequality (39). It is clear that

$$\begin{aligned}
\|\phi - \phi_I\|_0^2 &= (\int_\Omega |\phi - \phi_I|^2 dx) = (\sum_{\tau\in\Im_h} \int_\tau |\phi - \phi_I|^2 dx) \\
&\le \sum_{\tau\in\Im_h} |\phi - \phi_I|_{\infty,\tau} \int_\tau |\phi - \phi_I| dx \\
&\le \max_{\tau\in\Im_h} \|\phi - \phi_I\|_{\infty,\tau} \sum_{\tau\in\Im_h} \|\phi - \phi_I\|_{0,\tau} (\int_\tau 1 dx)^{\frac{1}{2}}, \text{ by the Hölder inequality,} \\
&\le \max_{\tau\in\Im_h} \|\phi - \phi_I\|_{\infty,\tau} \|\phi - \phi_I\|_0 |\Omega|, \text{ by the Schwartz inequality.}
\end{aligned}$$

By theorem 3.1, this implies $\|\phi - \phi_I\|_0 \le ch^2 \|\phi\|_2$, where c depends on $|\Omega|$ and $\max\{1/\rho, \rho\}$. Next, we show the estimation (40). It is well known that the inequality

$$\|\phi - \phi_I\|_{1,\tau} \le h\|\phi\|_{2,\tau} \quad (41)$$

holds, for elements $\tau \in \overset{\circ}{\Im}_h$ that do not intersect with interface. For an element $T \in \breve{\Im}_h$ that intersects with the interface, we have

$$\int_T \nabla(\phi - \phi_I)\nabla(\phi - \phi_I) dx = \underbrace{\int_{T\setminus T^*} \nabla(\phi - \phi_I)\nabla(\phi - \phi_I) dx}_{I} + \underbrace{\int_{T^*} \nabla(\phi - \phi_I)\nabla(\phi - \phi_I) dx}_{II} .$$

By Theorem 3.1, we can clearly see that,

$$\begin{aligned}(I) &\leq \|\nabla(\phi-\phi_I)\|_{\infty,T}\int_{T\setminus T^*} 1\cdot\sqrt{\nabla(\phi-\phi_I)\nabla(\phi-\phi_I)}dx\\ &\leq c_8 h|T|\|\nabla(\phi-\phi_I)\|_{0,T\setminus T^*}\left\|D^2\phi\right\|_{\infty,T},\end{aligned} \tag{42}$$

and

$$\begin{aligned}(II) &\leq \|\nabla(\phi-\phi_I)\|_{\infty,T^*}\int_{T^*} 1\cdot\sqrt{\nabla(\phi-\phi_I)\nabla(\phi-\phi_I)}dx\\ &\leq \|\nabla(\phi-\phi_I)\|_{\infty,T}\|\nabla(\phi-\phi_I)\|_{0,T^*}|T^*|.\end{aligned} \tag{43}$$

Recall that Γ denotes the approximate line segment of the interface $\tilde{\Gamma}$ in an element. Let M be an arbitrary point in $\tilde{\Gamma}_T$ and $M^{\perp}$ be the orthogonal projection of M onto the line segment Γ. Based on the assumption (H_3), $\tilde{\Gamma}$ can be represented by a C^2 function in each element. It has been shown in [26] that there exists a constant $\tilde{c}$ such that $\|M-M^{\perp}\|<\tilde{c}h^2$. We can see clearly that,

$$|T^*| = \int_0^{|\Gamma|}|\tilde{\Gamma}(s)-\Gamma(s)|ds \leq \tilde{c}h^3. \tag{44}$$

Plugging (44) into (43), and using Theorem 3.1, we can get

$$(II)\leq \tilde{c}h|T|\left\|D^2\phi\right\|_{\infty,T}\|\nabla(\phi-\phi_I)\|_{0,T^*}. \tag{45}$$

Combining (42) and (45), we have

$$\|\nabla(\phi-\phi_I)\|_{0,T}\leq \bar{c}h|T.|\left\|D^2\phi\right\|_{\infty,T} \tag{46}$$

Finally, from (41) and (46), we have

$$\begin{aligned}\|\phi-\phi_I\|_1^2 &\leq \left(\sum_{\tau\in\Im_h}\|\nabla(\phi-\phi_I)\|_{0,\tau}{}^2\right)^{1/2}\\ &\leq \bar{c}h\left(\sum_{\tau\in\Im_h}|\tau|^2\right)^{1/2}\|\phi-\phi_I\|_1\left\|D^2\phi\right\|_{\infty}.\end{aligned}$$

here $\bar{c}$ depends on $\max\{\rho, c1/\rho\}$ and $|\Omega|$. As a result, the inequality (40) holds. □

Remark 3.3 *Let u and u_h^I denote the weak solution and the IFE solution of the interface problem (1) on the mesh $\Im_h$. The a priori error estimate*

$$\left\|u - u_h^I\right\|_0 \leq ch^2 \left\|u\right\|_2 \text{ and } \left\|u - u_h^I\right\|_\beta \leq ch \left\|u\right\|_2$$

follows directly from the interpolation error estimates in theorem 3.2 and the Galerkin orthogonal property.

To obtain posteriori error estimations, we follow Verfürth's work in [4]. By using the seminal inequalities, we know that

$$\begin{cases} \|v\|_{0,\tau} \leq \gamma_1 \left\|\psi_\tau^{\frac{1}{2}} v\right\|_{0,\tau}, \\ \|\psi_\tau v\|_{1,\tau} \leq \gamma_2 h_\tau^{-1} \|v\|_{0,\tau}, \\ \|\sigma\|_{0,e} \leq \gamma_3 \left\|\psi_e^{\frac{1}{2}} \sigma\right\|_{0,e}, \\ \|\psi_e \sigma\|_{1,\tau} \leq \gamma_4 h_e^{-\frac{1}{2}} \|\sigma\|_{0,e}, \\ \|\psi_e \sigma\|_{0,\tau} \leq \gamma_5 h_e^{\frac{1}{2}} \|\sigma\|_{0,e}. \end{cases} \tag{47}$$

where v and σ are arbitrary polynomials of degree k, Verfürth has proposed an residual-based a posteriori error indicator and shown that, for the finite element solutions on an interface fitting grid, the effective constant between the local lower bound and the global upper bound is independent with the ratio $\rho = \frac{\beta^-}{\beta^+}$ of the flux jump across the interface. The analysis can be extended to higher order finite elements approximation as mentioned in [4]. In the following, we would like to show that with minor modification on the Verfürth's error indicator, the same estimates hold for the IFE solution.

Let $\varsigma = u - u_h^I$ and $\varsigma_\pi = I_\pi \varsigma$ be the quasi-interpolant of ς in $S_h(\Omega)$. By the theorem 2.1, there exist $\varsigma_\pi^I \in S_h^I(\Omega)$ such that $\varsigma_\pi^I(z) = \varsigma_\pi(z)$ for all $z \in \cup_{\tau \in \breve{\Im}_h} N_\tau$. By the orthogonality of the IFE solutions, we have

$$\begin{aligned} \|u - u_h^I\|_\beta^2 &= \int_\Omega \beta \nabla(u - u_h^I) \nabla(u - u_h^I) \\ &= \int_\Omega \beta \nabla(u - u_h^I) \left[\nabla(\varsigma - \varsigma_\pi) + \nabla\varsigma_\pi^I + \nabla(\varsigma_\pi - \varsigma_\pi^I)\right] dx \\ &= \underbrace{\int_\Omega \beta \nabla(u - u_h^I) \nabla(\varsigma - \varsigma_\pi) dx}_{(III)} + \underbrace{\int_\Omega \beta \nabla(u - u_h^I) \nabla(\varsigma_\pi - \varsigma_\pi^I) dx}_{(IV)}. \end{aligned} \tag{48}$$

First, we estimate (III) by the following Verfürth argument:

$$\begin{aligned}
(III) &= \sum_{\tau\in\Im_h}\int_\tau(-div(\beta\nabla u)+div\beta\nabla u_h)(\varsigma-\varsigma_\pi)dx \\
&- \sum_{e\in\mathcal{E}_h}\int_e[\beta\partial_h u_h]_e(\varsigma-\varsigma_\pi)ds \qquad (49)\\
&\le \sum_{\tau\in\Im_h}\mu_\tau\left\|f+div\beta\nabla u_h^I\right\|_{0,\tau}\mu_\tau^{-1}\left\|\varsigma-\varsigma_\pi\right\|_{0,\tau} \\
&+ \sum_{e\in\mathcal{E}_h}\mu_e^{\frac{1}{2}}\left\|\left[\beta\partial_n u_h^I\right]_e\right\|_{0,e}\mu_e^{-\frac{1}{2}}\left\|\varsigma-\varsigma_\pi\right\|_{0,e} \\
&\le \{\sum_{\tau\in\Im_h}\mu_\tau^2\left\|f+div\beta\nabla u_h^I\right\|_{0,\tau}^2+\sum_{e\in\mathcal{E}_h}\mu_e\left\|\left[\beta\partial_n u_h^I\right]\right\|_{0,e}^2\}^{\frac{1}{2}} \\
&\quad \{\sum_{\tau\in\Im_h}\mu_\tau^{-2}\left\|\varsigma-\varsigma_\pi\right\|_{0,\tau}^2+\sum_{e\in\mathcal{E}_h}\mu_e^{-1}\left\|\varsigma-\varsigma_\pi\right\|_{0,e}^2\}^{\frac{1}{2}},
\end{aligned}$$

here, μ_τ and μ_e are parameters to be determined. It has been shown in [4] that the following inequalities

$$\left\|\varsigma-\varsigma_\pi\right\|_{0,\tau} \le c_1 h_\tau\beta_\tau^{-\frac{1}{2}}\left\|\varsigma\right\|_{\beta,\tilde{\omega}_\tau} \qquad (50)$$

$$\left\|\varsigma-\varsigma_\pi\right\|_{0,e} \le c_2 h_e^{\frac{1}{2}}\beta_e^{-\frac{1}{2}}\left\|\varsigma\right\|_{\beta,\omega_e}, \qquad (51)$$

hold, where $\beta_e=\max_{\partial\tau_1\cap\partial\tau_2=e}\{\beta_{\tau_1},\beta_{\tau_2}\}$. Combining the estimates (49)-(51), an estimation of (III) independent with the diffusive coefficients can be derived for the interface fitted grids by choosing $\mu_\tau=h_\tau\beta_\tau^{-\frac{1}{2}}$ and $\mu_e=h_e\beta_e^{-1}$ in (49). Therefore, by partition the mesh $\breve{\Im}_h$ into a regular interface fitted mesh and applying the zero flux jump condition on the interface Γ, we can easily show that the inequality (49) implies

$$(III)\le c_{III}\{\sum_{\tau\in\Im_h}\mu_\tau^2\left\|f+div\beta\nabla u_h^I\right\|_{0,\tau}^2+\sum_{e\in\mathcal{E}_h}\mu_e\left\|\left[\beta\partial_n u_h^I\right]_e\right\|_{0,e}^2\}^{\frac{1}{2}}\left\|\varsigma\right\|_\beta, \quad (52)$$

where, for the element $\tau\in\breve{\Im}_h$ with $\tau=\tau^+\cup\tau^-$,

$$\mu_\tau^2\left\|f+div\beta\nabla u_h^I\right\|_{0,\tau}^2=h_\tau^2(\beta^+)^{-1}\left\|f+div\beta^+\nabla u_h^I\right\|_{0,\tau^+}^2+h_\tau^2(\beta^-)^{-1}\left\|f+div\beta^-\nabla u_h^I\right\|_{0,\tau^-}^2,$$

for the edge $e\in\breve{\mathcal{E}}$ with $e=e^+\cup e^-$, here $e^+\subset\partial\tau^+\setminus\Gamma$ and $e^-\subset\partial\tau^-\setminus\Gamma$,

$$\mu_e\left\|\left[\beta\partial_n u_h^I\right]_e\right\|_{0,e}^2=h_e(\beta^+)^{-1}\left\|\left[\beta^+\partial_n u_h^I\right]_{e^+}\right\|_{0,e^+}^2+(h_e\beta^-)^{-1}\left\|\left[\beta^-\partial_n u_h^I\right]_{e^-}\right\|_{0,e^-}^2.$$

Next, we estimate (IV). By employing the usual homogenization arguments and the inequalities (18) in the remark 2.2, we have

$$\begin{aligned}
\left\|\varsigma_\pi - \varsigma_\pi^I\right\|_{0,\tau} &\leq h_\tau \left\|\varsigma_\pi - \varsigma_\pi^I\right\|_{1,\tau} \leq c_1^I h_\tau \left\|\nabla \varsigma_\pi\right\|_{0,\tau} \\
&\leq c_1^I h_\tau \left(\left\|\nabla(\varsigma_\pi - \varsigma)\right\|_{0,\tau} + \left\|\nabla \varsigma\right\|_{0,\tau}\right) \qquad (53) \\
&\leq c_1^I \left(\left\|\varsigma_\pi - \varsigma\right\|_{0,\tau} + \beta^{-\frac{1}{2}} h_\tau \left\|\varsigma\right\|_{\beta,\tau}\right), \text{ by the inverse estimation,} \\
&\leq c_1^I h_\tau \beta^{-\frac{1}{2}} \left\|\varsigma\right\|_{\beta,\tilde{\omega}_\tau}, \text{by (50),}
\end{aligned}$$

where the constant $c_1^I = O(\max\{\rho, 1/\rho\})$. Similarly, by invoking the trace inequality, it can be shown that the following inequality holds

$$\left\|\varsigma_\pi - \varsigma_\pi^I\right\|_{0,e} \leq c_2^I h_e^{\frac{1}{2}} \beta_e^{-\frac{1}{2}} \left\|\varsigma\right\|_{\beta,\omega_e}, \qquad (54)$$

where $c_2^I = O(\max\{\rho, \frac{1}{\rho}\})$.

By following the same arguments in (49) and (52) with (50) and (51) replaced by (53) and (54), we can conclude that the following estimate holds:

$$(IV) \leq c_{IV}\{\sum_{\tau\in\Im_h} \mu_\tau^2 \left\|f + div\beta\nabla u_h^I\right\|_{0,\tau}^2 + \sum_{e\in\mathcal{E}_h} \mu_e \left\|\left[\beta\partial_n u_h^I\right]_e\right\|_{0,e}^2\}^{\frac{1}{2}} \left\|\varsigma\right\|_\beta, \quad (55)$$

where $C_{IV} = O(\max\{\rho, \frac{1}{\rho}\})$. The global a posteriori error bound then follows from the estimates (48), (52) and (55), and is stated in the following theorem.

Theorem 3.4 *Let u and u_h^I be the solutions of the interface problem (1) in $H^1(\Omega)$ and $S_h^I(\Omega)$, respectively, and f_τ denote the piecewise constant of the L^2-projection of the function f on element τ. Let $\tau = \tau^+ \cup \tau^-$, for any element $\tau \in \breve{\Im}_h$, and $\partial^+\tau$ and $\partial^-\tau$ denote the sets of boundary line segments of the element τ that belong to the sets $\partial\tau^+ \setminus \Gamma$ and $\partial\tau^- \setminus \Gamma$, respectively. Assume that u has H^2 regularity on each element. There exist a constant c_p independent with the diffusive coefficients such that the following a posteriori error bound holds.*

$$\left\|u - u_h^I\right\|_\beta \leq c_p\{\sum_{\tau\in\Im_h} [\eta_\tau^2 + h_\tau^2 \beta_\tau^{-1} \left\|f - f_\tau\right\|_{0,\tau}]\}^{\frac{1}{2}}, \qquad (56)$$

where

$$\eta_\tau = \left\{ h_\tau^2 \beta_\tau^{-1} \left\| f_h + div \beta_\tau \nabla u_h^I \right\|_{0,\tau}^2 + \frac{1}{2} \sum_{e \in \partial\tau} h_e \beta_\tau^{-1} \left\| \beta_\tau \left[\partial_{n_e} u_h^I \right] \right\|_{0,e}^2 \right\}^{\frac{1}{2}},$$

for $\tau \in \mathring{\Im}_h$, *and*

$$\eta_\tau = \left\{ \max\{\rho, \frac{1}{\rho}\} \left(\sum_{\tau' \in \{\tau^+, \tau^-\}} h_{\tau'}^2 \beta_{\tau'}^{-1} \left\| f_h + div \beta_{\tau'} \nabla u_h^I \right\|_{0,\tau'}^2 + \frac{1}{2} \sum_{e' \in \{\partial^+\tau, \partial^-\tau\}} h_{e'} \beta_{e'}^{-1} \left\| \beta_{e'} \left[\partial_{n_{e'}} u_h^I \right] \right\|_{0,e'}^2 \right) \right\}^{\frac{1}{2}},$$

for $\tau \in \breve{\Im}_h$, *here* $\beta_{e'} = \begin{cases} \beta^+ & \text{if } e' \in \partial^+\tau \\ \beta^- & \text{if } e' \in \partial^-\tau \end{cases}$.

4 Numerical examples

We now present some numerical results that support our theoretical results. Errors in the L^2 and H^1 norms of the IFE solutions to an interface problem will be given both on uniform triangular meshes and adaptively refined meshes. For simplicity, we solve the problem (1) in the rectangular domain $\Omega = (-1, 1) \times (-1, 1)$. The interface curve $\tilde{\Gamma}$ is a circle with radius $r_0 = 0.5$, which separates Ω into two subdomains Ω^- and Ω^+ with

$$\Omega^- = \{(x, y) : x^2 + y^2 \leq {r_0}^2\}.$$

The exact solution considered here is as following,

$$u(x, y) = \begin{cases} \dfrac{r^\alpha}{\beta^-}, & \text{if } r \leq r_0, \\ \dfrac{r^\alpha}{\beta^-} + (\dfrac{1}{\beta^-} - \dfrac{1}{\beta^+}) {r_0}^\alpha & \text{otherwise,} \end{cases} \tag{57}$$

where $r = \sqrt{x^2 + y^2}$, α = 3 and $\beta(x, y) = \begin{cases} \beta^-, & (x, y) \in \Omega^- \\ \beta^+, & (x, y) \in \Omega^+ \end{cases}$.

h	$\frac{\beta_1^-}{\beta_1^+} = 10^{-1}$	$\frac{\beta_2^-}{\beta_2^+} = 10^{-2}$	$\frac{\beta_3^-}{\beta_3^+} = 10^{-3}$
$\frac{1}{8}$	3.689e-03	3.676e-03	4.164e-03
$\frac{1}{16}$	9.897e-04	9.998e-04	1.110e-03
$\frac{1}{32}$	2.700e-04	2.673e-04	3.370e-04
$\frac{1}{64}$	6.766e-05	6.318e-05	7.567e-05

Table 1: Errors for problems with various diffusive coefficients in the L^2 norm.

The interface problems demonstrated here have diffusive coefficients:

$$\beta_k(x,y) = \begin{cases} 1, & (x,y) \in \Omega^- \\ 10^k, & (x,y) \in \Omega^+ \end{cases}, k = 1 \cdots 3.$$

A sample uniform mesh and adaptive mesh over the domain Ω with the interface curve $\tilde{\Gamma}$, together with a typical IFE solution on the adaptive mesh for the case $\beta^+ = 1000$ and $\beta^- = 1$, are shown in figure 3. Tables 1 and 2 contains the errors of the IFE solutions in the L^2 norm and the energy norm, respectively, on uniform meshes with grid size varies from $\frac{1}{8}$ to $\frac{1}{64}$. Using linear regression, we can see that the data in the table 1 obey

$$\left\|u - u_h^I\right\|_0 \approx 0.25h^{1.97}, \ \left\|u - u_h^I\right\|_0 \approx 0.27h^{2.00} \text{ and, } \left\|u - u_h^I\right\|_0 \approx 0.28h^{1.96},$$

and the data in the table 2 obey

$$\left\|u - u_h^I\right\|_{\beta_1} \approx 1.71h^{1.05}, \ \left\|u - u_h^I\right\|_{\beta_2} \approx 6.89h^{1.30}, \text{ and } \left\|u - u_h^I\right\|_{\beta_3} \approx 6.75h^{1.00}.$$

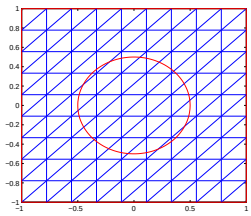

(a) uniform mesh

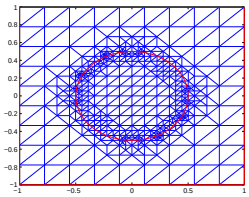

(b) adaptive mesh after 3 refinement

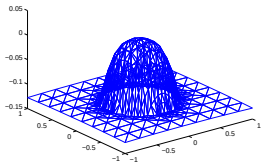

(c) Solution u on the adaptive mesh

Figure 3:

h	$\frac{\beta_1^-}{\beta_1^+} = 10^{-1}$	$\frac{\beta_2^-}{\beta_2^+} = 10^{-2}$	$\frac{\beta_3^-}{\beta_3^+} = 10^{-3}$
$\frac{1}{8}$	1.922e-01	4.677e-01	1.471e-00
$\frac{1}{16}$	8.314e-02	1.439e-01	4.390e-01
$\frac{1}{32}$	4.526e-02	8.726e-02	2.686e-01
$\frac{1}{64}$	2.222e-02	2.942e-02	8.394e-02

Table 2: Errors for problems with various diffusive coefficients in the energy norm.

These results clearly indicate that the IFE solutions u_h^I converge to the exact solution u with convergence rates $O(h^2)$ and $O(h)$ in the L^2 norm and the energy norm, respectively, as mentioned in the remark 3.3.

$\lvert N_h\rvert$	$\left\lVert u - u_h^I \right\rVert_\beta$	$(\sum_{\tau\in\Im_h} \eta_\tau^2)^{1/2}$
324	1.922e-01	4.117e-00
557	1.338e-01	2.316e-00
899	1.217e-01	1.756e-00
2516	6.281e-02	1.054e-00
3527	6.116e-02	7.515e-01
10482	3.097e-02	3.842e-01

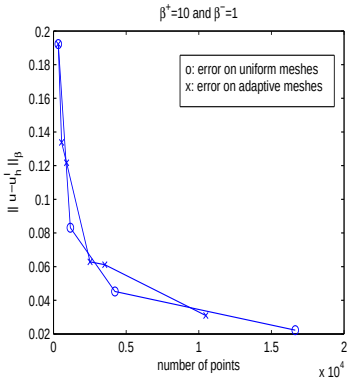

Figure 4: The errors in the energy norm and the a posteriori error bounds on adaptive meshes for the case $\beta^+ = 10$ and $\beta^- = 1$.

$\lvert N_h \rvert$	$\left\lVert u - u_h^I \right\rVert_\beta$	$(\sum_{\tau \in \Im_h} \eta_\tau^2)^{1/2}$
324	4.677e-01	1.136e+01
466	1.958e-01	1.538e+01
682	1.341e-01	2.280e-00
1507	5.495e-02	1.088e-00
4171	3.139e-02	5.201e-01
10243	2.188e-02	3.134e-01

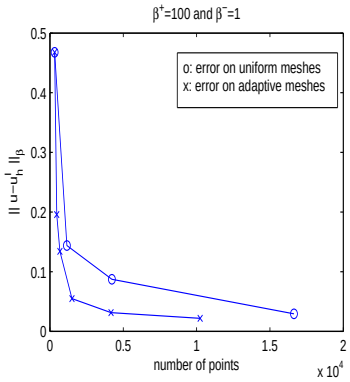

Figure 5: The errors in the energy norm and the a posteriori error bounds on adaptive meshes for the case $\beta^+ = 100$ and $\beta^- = 1$.

$\lvert N_h \rvert$	$\left\lVert u - u_h^I \right\rVert_\beta$	$(\sum_{\tau \in \Im_h} \eta_\tau^2)^{1/2}$
324	1.471e-00	1.592e+02
410	6.378e-01	1.659e+02
626	5.332e-01	8.339e-00
1066	2.057e-01	3.673e-00
1923	1.251e-01	1.572e-00
4021	4.105e-02	6.986e-01

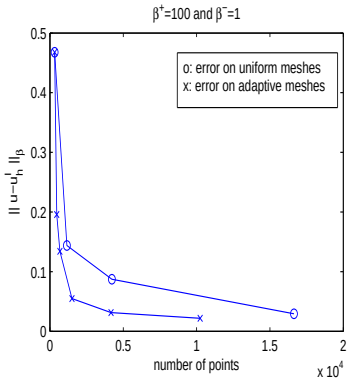

Figure 6: The errors in the energy norm and the a posteriori error bounds on adaptive meshes for the case $\beta^+ = 1000$ and $\beta^- = 1$.

Next, we compute the IFE solutions for the cases β_k, $k = 1 \cdots 3$ on adaptively refined meshes. To generate the adaptive meshes, the heuristic maximum marking strategy with threshold value 0.25 is employed. An element $\tau \in \Im_h$ will be marked for refinement if the associated error indicator value $\eta_\tau > 0.25 \max_{\tau' \in \Im_h} \eta_{\tau'}$. A regular mesh refinement scheme divides each marked triangle into 4 child triangles. Here, six levels of regular mesh refinement are performed on an initial 9×9 mesh. The tables on the left of the Figures 4, 5 and 6 contains the errors of the IFE solutions in the energy norms and the a posteriori error bounds defined in the theorem 3.4 on the adaptive meshes. Comparisons of the errors on uniform meshes

and adaptive meshes are shown on the right in each figure. From these figures, we can see that, on adaptive meshes, the accuracy of the IFE solutions is significantly increased and much less grid points are needed for the IFE solutions to reach a given error tolerance, when $\beta^+ \gg \beta^-$. In addition, the ratios of $(\sum_{\tau\in\Im_h} \eta_\tau^2)^{1/2}$ to $\left\|u - u_h^I\right\|_\beta$ tends to an order of 10 for all three cases when the number of mesh refinement is increased. This result suggests that the proposed a posteriori error bound in theorem 3.4 is indeed independent with the diffusive coefficients.

5 Conclusions

In this paper, we have developed an adaptive mesh refinement technique for the non-conforming immersed finite element (IFE) method. The underlying triangulation and local mesh refinement does not need to fit the interface. The accuracy of the solution and its gradient is significant improved with the local adaptive mesh refinement. Some improved a prior error estimate is also derived for the original non-conforming IFE method along with an a posteriori error estimation needed for the adaptive mesh refinement technique.

The first author was supported by the Taiwan NSC grant 97-2119-M-009-006. The second author was partially supported by the US ARO grants 56349MA-MA, and 550694-MA, the AFSOR grant FA9550-09-1-0520, and US NSF grant DMS-0911434. The first author C-T. Wu would like to thank Dr. Zhilin Li and North Carolina State University for the hospitality during the author's visit. The research was initiated by the visit.

References

[1] I. Babuška and W. C. Rheinboldt. Error estimates for adaptive finite element computations. *SIAM J. Numer. Anal.*, 15:736–754, 1978.

[2] R. E. Bank and A. Weiser. Some a posteriori error estimators for elliptic partial differential equations. *Math. Comp.*, 44:283–301, 1985.

[3] J. W. Barrett and C. M. Elliott. Fitted and unfitted finite element methods for elliptic equations with smooth interfaces. *IMA J. Numer. Anal.*, 7:283–300, 1987.

[4] C. Bernardi and R. Verfürth. Adaptive finite element methods for elliptic equations with non-smooth coefficients. *Numer. Math.*, 85:579–608, 2000.

[5] J. H. Bramble and J. T. King. A finite element method for interface problems in domains with smooth boundary and interfaces. *Advances in Comp. Math.*, 6:109–138, 1996.

[6] Z. Chen and J. Zou. Finite element methods and their convergence for elliptic and parabolic interface problems. *Numer. Math.*, 79:175–202, 1998.

[7] RW Clough and JL Toucher. Finite element stiffness matrices for analysis of plate bending. *Proceeding of Conference on Matrix Methods in Structural Mechanics, WPAFB, Ohio*, pages 515–545, 1965.

[8] A. Hansbo and P. Hansbo. An unfitted finite element method, based on nitsche's method, for elliptic interface problems. *Comp. Methods Appl. Mech. Engrg.*, 191:5537–5552, 2002.

[9] R. J. Leveque and Z. Li. The immersed interface method for elliptic equations with discontinuous coefficients and singular sources. *SIAM J Numer Anal*, 31:1019–1044, 1994.

[10] R. J. Leveque and Z. Li. Immersed interface method for stokes flow with elastic boundaries for source tension. *SIAM J Sci Comput*, 18:709–735, 1997.

[11] Z. Li and J. Zou. Theoretical and numerical analysis on a thermo-elastic system with discontinuities. *J Comput Appl Math 91 (1998), 1-22.*, 91:1–22, 1998.

[12] R. H. Nochetto P. Morin and K. Siebert. Data oscillation and convergence of adaptive fem. *SIAM J. Numer. Anal.*, 38:466–488, 2000.

[13] A. Papastavrou and R. Verfürth. A posteriori error estimators for stationary convection-diffusion problems: a computational comparison. *Comput. Methods Appl. Mech. Engrg.*, 189:449–462, 2000.

[14] T. Lin R. Ewing, Z. Li and Y. Lin. The immersed finite volume element methods for the elliptic interface problems. *Math Comput Simul*, 50:63–76, 1999.

[15] M. C. Rivara. Algorithms for refining triangular grids suitable for adaptive and multigrid techniques. *Int. J. Numer. Methods Eng.*, 20:745–756, 1984.

[16] M. C. Rivara. Using longest-side bisection techniques for the automatic refinement of Delaunay triangulation. *Int. J. Numer. Methods Eng.*, 40:581–597, 1997.

[17] S. Osher T. Hou, Z. Li and H. Zhao. A hybrid method for moving interface problems with application to the hele-shaw flow. *J Comput Phys*, 134:234–252, 1997.

[18] T.Lin and J. Wang. An immersed finite element electric field solver for ion optics modeling. *Proceeding of AIAA Joint Propulsion Conference, Indianapolis, IN*, AIAA:2002–4263, 2002.

[19] T.Lin and J. Wang. An immersed finite element method for plasma particle simulation. *Proceeding of AIAA Aerospace Science Meeting, Reno, NV*, AIAA:2003–0842, 2003.

[20] R. Verfürth. A review of posteriori error estimation and adaptive mesh-refinement techniques. *Wiley and Teubner*, 1996.

[21] R. Verfürth. A posteriori error estimators for convection-diffusion equations. *Numer. Math.*, 80:641–663, 1998.

[22] A. Wiegmann and K. Bube. The immersed interface method for nonlinear differential equations with discontinuous coefficients and singular sources. *SIAM J Numer Anal 35 (1998), 177-200.*, 35:177–200, 1998.

[23] Bo Li Yan Gong and Z. Li. Immersed interface finite element methods for elliptic interface problems with nonhomogeneous jump conditions. *SIAM J. Numer. Anal.*, 46:472–495, 2008.

[24] D. McTigue Z. Li and J. Heine. A numerical method for diffysive transport with moving boundaries and discontinuities material properties. *Int J Numer Anal Method Geomesh*, 21:653–672, 1997.

[25] T. Lin Z. Li and X.Wu. New cartesian grid methods for interface problems using finite element formulation. *Numer. Math.*, 96:61–98, 2003.

[26] Y. Lin Z. Li, T. Lin and R. C. Roger. An immersed finite element space and its approximation capability. *Numerical Methods of PDEs*, 20:338–367, 2004.

[27] O. C. Zienkiewicz and J. Z. Zhu. Adaptivity and mesh generation. *Int. J. Numer. Methods. Engrg.*, 32:783–810, 1991.